Core collapse in massive scalar-tensor gravity

Roxana Rosca-Mead[1,*] Ulrich Sperhake[1,2,†] Christopher J. Moore[3,‡] Michalis Agathos[1,4,§]
Davide Gerosa[3,‖] and Christian D. Ott[5,¶]

[1]*DAMTP, Centre for Mathematical Sciences, University of Cambridge,*
Wilberforce Road, Cambridge CB3 0WA, United Kingdom
[2]*TAPIR 350-17, California Institute of Technology,*
1200 E. California Blvd., Pasadena, California 91125, USA
[3]*School of Physics and Astronomy & Institute for Gravitational Wave Astronomy,*
University of Birmingham, Birmingham B15 2TT, United Kingdom
[4]*Kavli Institute for Cosmology Cambridge, Madingley Road, Cambridge CB3 0HA, United Kingdom*
[5]*OCS Labs LLC, Pasadena, California 91104, USA*

This paper provides an extended exploration of the inverse-chirp gravitational-wave signals from stellar collapse in massive scalar-tensor gravity reported in [Phys. Rev. Lett. **119**, 201103]. We systematically explore the parameter space that characterizes the progenitor stars, the equation of state, and the scalar-tensor theory of the core collapse events. We identify a remarkably simple and straightforward classification scheme of the resulting collapse events. For any given set of parameters, the collapse leads to one of three end states: a weakly scalarized neutron star, a strongly scalarized neutron star, or a black hole, possibly formed in multiple stages. The latter two end states can lead to strong gravitational-wave signals that may be detectable in present continuous-wave searches with ground-based detectors. We identify a very sharp boundary in the parameter space that separates events with strong gravitational-wave emission from those with negligible radiation.

I. INTRODUCTION

Black holes (BHs) and neutron stars (NSs) populate the graveyard of massive stars. As the star's iron core exceeds its effective Chandrasekhar mass, gravitational instability causes collapse to a NS. Collapse is initially halted by the repulsive character of nuclear interactions, causing the inner core to bounce. This bounce may liberate a hydrodynamical shock that will propagate through the star's envelope and eventually result in a supernova. For some progenitors, further accretion from the star's outer layers can then turn the NS into a BH.

The formation of BHs and NSs via stellar collapse naturally involves strong, dynamical gravitational fields, thus constituting a precious tool to investigate the nature of gravity [1]. In particular, core collapse is ideal to constrain those generalizations of Einstein's general relativity (GR) where compact objects present a substantially different structure. Examples of these are spontaneously scalarized NSs [2–5] and BHs [6,7] in some classes of scalar-tensor (ST) theories, universal horizons in theories with Lorentz violation [8], or

the spontaneous growth of vector or tensor fields around compact objects in modified gravity [9–11].

Probing the dynamics and gravitational-wave (GW) emission of compact objects undergoing such dynamic processes requires a well-posed formulation of the underlying theory that allows for implementation in numerical evolution codes. The demonstration of the well-posedness of GR by Choquet-Bruhat [12,13] represents a milestone in the mathematical understanding of Einstein's theory, and the corresponding problem is now being tackled for some of the most popular alternative theories of gravity [14–18].

ST theories, where gravity is mediated by the usual graviton and an additional scalar field, are arguably the simplest and most intensively studied generalization of GR. Extending early seminal work by Brans and Dicke [19], the theory's most general formulation was first written down by Horndeski [20]. These theories have been strongly tested in the weak-field regime by the Cassini mission [21], Lunar Laser Ranging [22], and binary pulsars [23]. ST theories of gravity are now being severely constrained by GW observations [24,25]. In particular, the multimessenger observation of GW170817 [26] has ruled out all variants of Horndeski theory where the speed of photons and gravitons differs by more than $\sim 5 \times 10^{-16}$ [27–29]. For some Horndeski theories, gravity has a dispersion relation (i.e., waves with different frequencies travel at different speeds)

[*]rr417@cam.ac.uk
[†]u.sperhake@damtp.cam.ac.uk
[‡]cmoore@star.sr.bham.ac.uk
[§]magathos@damtp.cam.ac.uk
[‖]d.gerosa@bham.ac.uk
[¶]christian.d.ott@gmail.com

which provides a further handle to constrain the nature of gravity with GW signals.

In this paper, we study BH and NS formation in a particular subclass of massive scalar-tensor (MST) gravity and explore its consequences for current and future GW observations. We note in this context that the above mentioned constraints on the propagation of GWs apply to the spin-two modes but do not, as yet, constrain the propagation speed and, hence, the mass of scalar degrees of freedom. In particular, the ST formulation by Refs. [2,30,31] with the addition of a mass term (e.g., [3]) constitute an ideal playground for probing additional physics with stellar collapse [32–40]. This class of ST theories presents three crucial features:

(1) The Einstein frame reduction (see, e.g., [41]) immediately proves that the theory is well-posed and thus suitable to be tackled by numerical integration.

(2) A new family of stationary NS solutions is present, which are macroscopically different from their GR counterparts [2].

(3) The presence of a nonzero scalar-field mass introduces a dispersion relation, with a consequent new phenomenology for the emitted GW signal.

With these ingredients in the blender, our previous contribution [35,37,39] has presented a limited suite of simulations of NS and BH formation from realistic presupernova stellar density profiles and highlighted the presence of characteristic "inverse GW chirp" signals. Encoded in the oscillation of the scalar field, high-frequency GW signals reach the detector sooner compared to low-frequency modes. Signals might still be present for decades, or even centuries, after the core collapse event, thus providing us with the tantalizing possibility of testing massive ST theories with GW observations of historic supernovae.

In this paper, we extend our previous work by presenting a systematic exploration of the phenomenology of core collapse in massive ST gravity. In Sec. II, we review the complete formalism used in this study, including equations of motions in flux-conservative form and details on the equation of state. In Sec. III, we summarize our numerical implementation, including initial data and the evolution scheme. Section IV presents a complete taxonomy of the collapse process and its end points.

A surprisingly simple picture emerges: despite the large dimensionality of the problem, the collapse dynamics can always be classified as one of only five possible scenarios. These are the following: (i) single-stage collapse to GR-like NSs, (ii) collapse to a BH following one accretion episode, (iii) collapse to a BH following multiple accretion and proto-NS stages, (iv) collapse to a strongly scalarized NS via accretion onto a GR-like proto-NS, and (v) direct collapse to a strongly scalarized NS.

We then proceed by analyzing the GW consequences of our findings. Section V provides a careful derivation and analysis of the inverse-chirp signal morphology.

In particular, we argue that the features depend only on the mass of the scalar field and not the details of the source dynamics. Moreover, the main characteristics of the GW signal, its frequency and amplitude as functions of time, depend (to good accuracy) on the scalar mass only through a remarkably simple rescaling. In Sec. VI we present the relevance of our simulations to current and future GW searches. Finally, in Sec. VII we draw our conclusions. To streamline the flow of the paper, several details are postponed to the Appendixes. In particular, Appendix A provides a more detailed description of each collapse scenario through the analysis of a representative example. Appendix B illustrates more results on the impact of the equation of state and progenitor model on the degree of scalarization. The accuracy of the stationary-phase approximation in describing the propagation of massive scalar waves is verified through a numerical test in Appendix C, and Appendix D provides more results on the LIGO detectability of the inverse-chirp signal.

Overall, this paper contains the results of $\mathcal{O}(4 \times 10^3)$ one-dimensional (1D) core-collapse simulations for a total computational time of $\mathcal{O}(2 \times 10^6)$ CPU hours. Throughout this paper we use geometric units $c = G = 1$.

II. SCALAR-TENSOR THEORY

In this work we consider the class of scalar-tensor theories of gravity first studied by Bergmann [30] and Wagoner [31], which satisfy the following assumptions:

(1) The equations of motion are derived from the variation of an action $S = S_G + S_M$ where S_G consists exclusively of the gravitational fields and S_M represents the interaction of gravity with all matter fields.

(2) All long-range forces are mediated by the three lowest-spin bosons. Electromagnetism is the only spin one interaction and the spin zero contribution is described by a single real scalar field.

(3) Variation of the action results in at most two-derivative field equations, i.e., terms linear in second derivatives or quadratic in first derivatives or of lower order.

(4) The theory is diffeomorphism invariant, i.e., formulated in terms of tensorial equations.

(5) The weak equivalence principle is satisfied.

Using the above principles, we can formulate the action in the Jordan-Fierz frame [1]:

$$S = \int dx^4 \sqrt{-g} \left[\frac{F(\phi)}{16\pi} R - \frac{1}{2} g^{\mu\nu} (\partial_\mu \phi)(\partial_\nu \phi) - W(\phi) \right] + S_M[\psi_m, g_{\mu\nu}], \tag{1}$$

where $g_{\mu\nu}$ represents the metric (from now on referred to as the Jordan metric), g is its determinant, R is the Ricci scalar corresponding to $g_{\mu\nu}$, ϕ represents the scalar field, F and W

are functions of ϕ, and S_M represents the action of the matter fields ψ_m. A particularly convenient (and in some instances preferable [42]) formulation of this class of theories is obtained in the so-called *Einstein frame*. This is achieved through a conformal transformation

$$\bar{g}_{\mu\nu} \equiv F(\phi)g_{\mu\nu}, \tag{2}$$

and a redefinition of the scalar field according to

$$\frac{\partial\varphi}{\partial\phi} = \sqrt{\frac{3}{4}\frac{F_{,\phi}^2}{F^2} + \frac{4\pi}{F}}; \tag{3}$$

for an exploration of the regime of viability of this transformation see [43]. The action of Bergmann-Wagoner scalar tensor theory is then given by [1,44]

$$S = \int d^4x \frac{\sqrt{-\bar{g}}}{16\pi}[\bar{R} - 2\bar{g}^{\mu\nu}\partial_\mu\varphi\partial_\nu\varphi - 4V(\varphi)]$$
$$+ S_M\left[\psi_m, \frac{\bar{g}_{\mu\nu}}{F}\right], \tag{4}$$

where $V(\varphi)$ is the scalar potential and $\bar{R}$ and $\bar{g}$, respectively, denote the Ricci scalar and determinant constructed from the conformal metric. Note that we recover Brans-Dicke theory [19] with the choice $F = \exp(-2\varphi/\sqrt{3 + 2\omega_{BD}})$ while general relativity corresponds to the trivial case $\varphi = \text{const}$.

In this work we choose the matter part of the action S_M such that the physical energy momentum tensor describes a perfect fluid with baryon density ρ, pressure P, internal energy ϵ, enthalpy H, and 4-velocity u^α,

$$T^{\mu\nu} \equiv \frac{2}{\sqrt{-g}}\frac{\delta S_M}{\delta g_{\mu\nu}} = \rho H u^\mu u^\nu + P g^{\mu\nu}. \tag{5}$$

The equations of motion are obtained through variation of the action (4) with respect to the metric, the scalar, and the matter fields, as well as the continuity equation for baryon conservation in the physical frame,

$$\bar{G}_{\alpha\beta} = 2\partial_\alpha\varphi\partial_\beta\varphi - \bar{g}_{\alpha\beta}\partial^\mu\varphi\partial_\mu\varphi + 8\pi\bar{T}_{\alpha\beta} - 2V\bar{g}_{\mu\nu}, \tag{6}$$

$$\bar{\nabla}^\mu\bar{\nabla}_\mu\varphi = 2\pi\frac{F_{,\varphi}}{F}\bar{T} + V_{,\varphi}, \tag{7}$$

$$\bar{\nabla}_\mu\bar{T}^{\mu\alpha} = -\frac{1}{2}\frac{F_{,\varphi}}{F}\bar{T}\bar{g}^{\alpha\mu}\bar{\nabla}_\mu\varphi, \tag{8}$$

$$\nabla_\mu(\rho u^\mu) = 0. \tag{9}$$

Here $\bar{T}_{\alpha\beta} = T_{\alpha\beta}/F$ is the conformal energy momentum tensor, $\bar{\nabla}$ and ∇ are the covariant derivatives associated

with $\bar{g}_{\mu\nu}$ and $g_{\mu\nu}$, respectively, and the subscript $,\varphi$ denotes differentiation with respect to φ.

The specific scalar-tensor theory of gravity is determined by the choice of the potential function $V(\varphi)$ and the conformal factor $F(\varphi)$. Here we consider a noninteracting scalar field with mass parameter μ, so that the potential is given by

$$V(\varphi) = \frac{\mu^2\varphi^2}{2\hbar^2}. \tag{10}$$

The scalar mass introduces a characteristic frequency

$$\omega_* = 2\pi f_* = \frac{\mu}{\hbar}. \tag{11}$$

Finally, we write the conformal factor as

$$F(\varphi) = e^{-2\alpha_0\varphi - \beta_0\varphi^2}, \tag{12}$$

where α_0 and β_0 are dimensionless parameters. This choice for the conformal factor (sometimes also written as $A \equiv F^{-1/2}$; cf. [45]) is very common in the literature and motivated by the fact that in this form α_0 and β_0 completely determine all modifications of gravity at first post-Newtonian order [45–47].

Henceforth, we consider spherical symmetry and impose polar slicing and radial gauge [48] in the Einstein frame, so that the line element takes on the form

$$d\bar{s}^2 = \bar{g}_{\mu\nu}dx^\mu dx^\nu = -F\alpha^2 dt^2 + FX^2 dr^2 + r^2 d\Omega^2, \tag{13}$$

where α and X are functions of (t, r). Following common practice, we introduce for convenience the potential $\Phi(t, r)$ and the mass function $m(t, r)$ through

$$F\alpha^2 = e^{2\Phi}, \qquad FX^2 = \left(1 - \frac{2m}{r}\right)^{-1}. \tag{14}$$

The four velocity in spherical symmetry is

$$u^\mu = \frac{1}{\sqrt{1 - v^2}}\left[\frac{1}{\alpha}, \frac{v}{X}, 0, 0\right], \tag{15}$$

where the velocity field v as well as the matter variables ρ, P, H, ϵ of Eq. (5) are functions of (t, r). By inserting the expressions of Eqs. (5) and (13)–(15) into the field equations (6)–(9), we obtain the set of equations that govern the dynamics of spherically symmetric fluid configurations in Bergmann-Wagoner ST theory of gravity. In order to accurately model discontinuities arising through shock formation in the fluid profiles, however, we require high resolution shock capturing and, hence, a flux conservative form of the matter equations. This is achieved by converting the *primitive* variables (ρ, v, H) to their flux conservative counterparts [35,49],

$$D = \frac{\rho X F^{-3/2}}{\sqrt{1-v^2}}, \quad S^r = \frac{\rho H v F^{-2}}{1-v^2}, \quad \tau = \frac{S^r}{v} - \frac{P}{F^2} - D. \quad (16)$$

Finally, we convert the wave equation (7) for the scalar field into a first order system by defining

$$\eta = \frac{1}{X} \partial_r \varphi, \quad \psi = \frac{1}{\alpha} \partial_t \varphi. \quad (17)$$

The final set of equations can then be written in the form

$$\partial_r \Phi = X^2 F \left[\frac{m}{r^2} + 4\pi r \left(S^r v + \frac{P}{F^2} \right) + \frac{r}{2F} (\eta^2 + \psi^2) \right] \\ - rFX^2 V, \quad (18)$$

$$\partial_r m = 4\pi r^2 (\tau + D) + \frac{r^2}{2F} (\eta^2 + \psi^2) + r^2 V, \quad (19)$$

$$\partial_t \varphi = \alpha \psi, \quad (20)$$

$$\partial_t \eta = \frac{1}{X} \partial_r (\alpha \psi) - rX\alpha \eta(\eta \psi - 4\pi F S^r) + \frac{F_{,\varphi}}{2F} \alpha \eta \psi, \quad (21)$$

$$\partial_t \psi = \frac{1}{r^2 X} \partial_r (r^2 \alpha \eta) - rX\alpha \psi(\eta \psi - 4\pi F S^r) + \frac{F_{,\varphi}}{2F} \alpha \psi^2 \\ + 2\pi\alpha \left(\tau - S^r v + D - 3\frac{P}{F^2} \right) F_{,\varphi} - \alpha F V_{,\varphi}, \quad (22)$$

$$\partial_t \begin{pmatrix} D \\ S^r \\ \tau \end{pmatrix} = \frac{1}{r^2} \partial_r \left[r^2 \frac{\alpha}{X} \begin{pmatrix} f_D \\ f_{S^r} \\ f_\tau \end{pmatrix} \right] = \begin{pmatrix} s_D \\ s_{S^r} \\ s_\tau \end{pmatrix}, \quad (23)$$

with fluxes and sources given by

$$f_D = Dv, \quad (24)$$

$$f_{S^r} = S^r v + \frac{P}{F^2}, \quad (25)$$

$$f_\tau = S^r - Dv, \quad (26)$$

$$s_D = -D\frac{F_{,\varphi}}{2F} \alpha(\psi + v\eta), \quad (27)$$

$$s_{S^r} = (S^r v - \tau - D)\alpha XF \left(8\pi r \frac{P}{F^2} + \frac{m}{r^2} - \frac{F_{,\varphi}}{2F^2 X} \eta - rV \right) \\ + \frac{\alpha X}{F} P \frac{m}{r^2} + 2\frac{\alpha P}{rXF^2} - r\alpha X\frac{P}{F} V \\ - 2r\alpha XS^r \eta\psi - \frac{3}{2}\alpha\frac{P}{F^2}\frac{F_{,\varphi}}{F}\eta \\ - \frac{r}{2}\alpha X(\eta^2 + \psi^2)\left(\tau + \frac{P}{F^2} + D \right)(1 + v^2), \quad (28)$$

$$s_\tau = -\left(\tau + \frac{P}{F^2} + D \right) r\alpha X[(1 + v^2)\eta\psi + v(\eta^2 + \psi^2)] \\ + \frac{\alpha}{2}\frac{F_{,\varphi}}{F}\left[Dv\eta + \left(S^r v - \tau + 3\frac{P}{F^2} \right)\psi \right]. \quad (29)$$

Note that these equations differ from Eqs. (2.21), (2.22), (2.26)–(2.28), and (2.33)–(2.39) in Ref. [35] through the presence of the potential terms involving V in our Eqs. (18), (19), (22), and (28). In particular, the principal part and the characteristic structure of the equations are identical to those in the case of a massless scalar field, and we consequently inherit the well-posed character of the evolution equations of the massless case.

In order to close the system of differential equations (18)–(29), we need to prescribe an equation of state (EOS) that provides the pressure as a function of ρ and ϵ. Here we use a so-called hybrid EOS introduced in Ref. [50] that captures in closed analytic form the stiffening of the matter at nuclear densities and models the response of shocked material through a thermal pressure component; see also Refs. [51–54] for comparisons with modern finite-temperature EOSs. The hybrid EOS consists of a cold and a thermal pressure component given by

$$P = P_c + P_{\rm th}. \quad (30)$$

The cold component has piecewise polytropic form

$$P_c = \begin{cases} K_1 \rho^{\Gamma_1} & \text{if } \rho \le \rho_{\rm nuc} \\ K_2 \rho^{\Gamma_2} & \text{if } \rho > \rho_{\rm nuc} \end{cases}, \quad (31)$$

and the thermal contribution is given by

$$P_{\rm th} = (\Gamma_{\rm th} - 1)\rho(\epsilon - \epsilon_c), \quad (32)$$

where ϵ is the internal energy and ϵ_c follows from the first law of thermodynamics for adiabatic processes,

$$\epsilon_c = \begin{cases} \frac{K_1}{\Gamma_1 - 1}\rho^{\Gamma_1 - 1} & \text{if } \rho \le \rho_{\rm nuc} \\ \frac{K_2}{\Gamma_2 - 1}\rho^{\Gamma_2 - 1} + E & \text{if } \rho > \rho_{\rm nuc} \end{cases}. \quad (33)$$

Prior to core bounce, the flow is adiabatic which implies $\epsilon \approx \epsilon_c$, but at core bounce the shocked material becomes nonadiabatical and thus subject to a non-negligible thermal pressure component.

We set the nuclear density $\rho_{\rm nuc} = 2 \times 10^{14} \, \text{g cm}^{-3}$ [52] and $K_1 = 4.9345 \times 10^{14}$ [cgs] as predicted for a relativistic degenerate gas of electrons with electron fraction $Y_e = 0.5$ [55]. The constants K_2 and E follow from continuity at $\rho = \rho_{\rm nuc}$. The EOS given by Eqs. (30)–(33) is thus determined by the three adiabatic indices Γ_1, Γ_2, and $\Gamma_{\rm th}$. A gas of relativistic electrons has an adiabatic index of 4/3, but electron capture during the collapse phase reduces the effective adiabatic index Γ_1 to slightly lower values in the range $\Gamma_1 \approx 1.28$ to $\Gamma_1 \approx 1.32$ [53,54,56]. At densities $\rho > \rho_{\rm nuc}$, however, the repulsive core of the nuclear force stiffens the EOS which leads to a larger adiabatic index Γ_2. Reference [54] find $\Gamma_2 \approx 2.5$ and $\Gamma_2 \approx 3$ to approximate well the finite-temperature EOSs of

TABLE I. Parameters for different hybrid equations of state. The noncontiguous EOS labels are due to the fact that we have also explored collapse configurations with EOSs using different combinations of the given parameter values. These simulations, without exception, fit into the classification scheme of Sec. IV and are therefore not reported here.

	EOS1	EOS3	EOS5	EOS8	EOSa
Γ_1	1.30	1.32	1.30	1.30	1.28
Γ_2	2.50	2.50	3.00	2.50	3.00
Γ_{th}	1.35	1.35	1.35	1.50	1.50

Lattimer-Swesty [57,58] and Shen *et al.* [59,60], respectively. Finally, the thermal adiabatic index Γ_{th} models a mixture of relativistic and nonrelativistic gas which leads to the bounds $4/3 < \Gamma_{th} < 5/3$.

Our hybrid EOS is therefore determined by three parameters. Motivated by the above considerations, we select values $\Gamma_1 \in \{1.28, 1.3, 1.32\}$, $\Gamma_2 \in \{2.5, 3\}$, and $\Gamma_{th} \in \{1.35, 1.5\}$ with $(\Gamma_1, \Gamma_2, \Gamma_{th}) = (1.3, 2.5, 1.35)$ as our fiducial model. In particular, we pick five different combinations of the EOS parameters as listed in Table I.

III. COMPUTATIONAL FRAMEWORK AND INITIAL DATA

We evolve the set of differential equations (18)–(23) with an extended version of the open-source code GR1D [49] originally developed for modeling stellar collapse in general relativity. GR1D has been generalized to massless scalar-tensor gravity in Ref. [35], and we have merely added to this version of the code the potential terms involving V or $V_{,\varphi}$ in Eqs. (18)–(29). As mentioned above, these terms do not change the characteristics of the differential equations and thus allow us to use the shock-capturing scheme in the very same form as in [35].

In order to capture the vastly different length scales encountered in our simulations, we employ a computational grid consisting of an inner grid with uniform resolution Δr_1 out to $r = 40$ km and an outer component with logarithmic spacing up to $r = 9 \times 10^5$ km, resulting in a total of N grid points. In Ref. [37], some of the authors have analyzed the convergence of the resulting core collapse simulations and found a discretization error in the wave signal of about 4% for a grid setup using $\Delta r_1 = 250$ m and $N = 10000$. This is the minimum resolution used for all the simulations of this work. Finally, we have verified that the error due to extracting the wave signal at a large but finite radius is negligible compared with the discretization error, and we therefore estimate the total numerical uncertainty as ∼4%.

All simulations presented in this work start with the nonrotating models of the catalog of spherically symmetric presupernova stars provided by Woosley and Heger [61]. These models have been obtained by evolving stars in Newtonian gravity up to the moment of iron core collapse and provide profiles for stars with zero-age-main-sequence (ZAMS) masses from 10.8 to 75 solar masses and three different metallicities: solar, 10^{-4} times solar, and primordial metallicity. Throughout this work, we denote the progenitor models by a prefix "*s*," "*u*," or "*z*," respectively, for the three metallicities, followed by the ZAMS mass. With this notation, for instance, "u39" denotes a progenitor with 10^{-4} times solar metallicity and mass $M_{ZAMS} = 39 M_{\odot}$. In the weak-gravity regime of these low-density progenitor stars (their central density is a factor about 10^5 below nuclear density), the scalar field is negligible, and we therefore set $\varphi = 0$ initially. The initial metric variables can then be computed directly from the matter profile using quadrature in Eqs. (18) and (19).

IV. PHENOMENOLOGY OF STELLAR COLLAPSE

A. Classification

Stellar core collapse and supernova explosions are highly complex processes, and the dynamics in numerical simulations can depend sensitively on the level of detail included in the modeling. The focus of our study is an exploration of the parameter space through a large number $[\mathcal{O}(4 \times 10^3)]$ of long simulations (several seconds). For computational feasibility, we consider nonrotating stars in spherical symmetry with piecewise polytropic EOS and do not consider neutrino transport. We characterize the progenitor stars in terms of their ZAMS mass and metallicity (the grid used in the progenitor catalog of [61]), but note the strong correlation of the outcome of a collapse event with the compactness of the stellar core at bounce [62]. While the qualitative picture from our simulations is robust, some caution is advised on the quantitative details; in particular the location of the boundaries between strongly and scalarized configurations in Figs. 3 and 4 may change under a refinement of the modeling framework.

Within our framework, a given stellar collapse model is characterized by eight parameters:
  (i) The EOS is characterized by two polytropic exponents Γ_1, Γ_2, and the thermal pressure coefficient Γ_{th}.
 (ii) The stellar progenitors are characterized by metallicity Z and zero-age-main-sequence mass M_{ZAMS}.
(iii) The ST theory of gravity is determined by the mass of the scalar field μ and the coefficients α_0 and β_0 entering the conformal factor.

Such a vast parameter space allows for an enormous phenomenology and, through sheer numbers, represents a major challenge for a numerical exploration; surmounting this challenge is the central goal of this section. More specifically, we will see that within our modeling framework, the phenomenology of the different collapse scenarios reveals distinct patterns and systematics that enable us
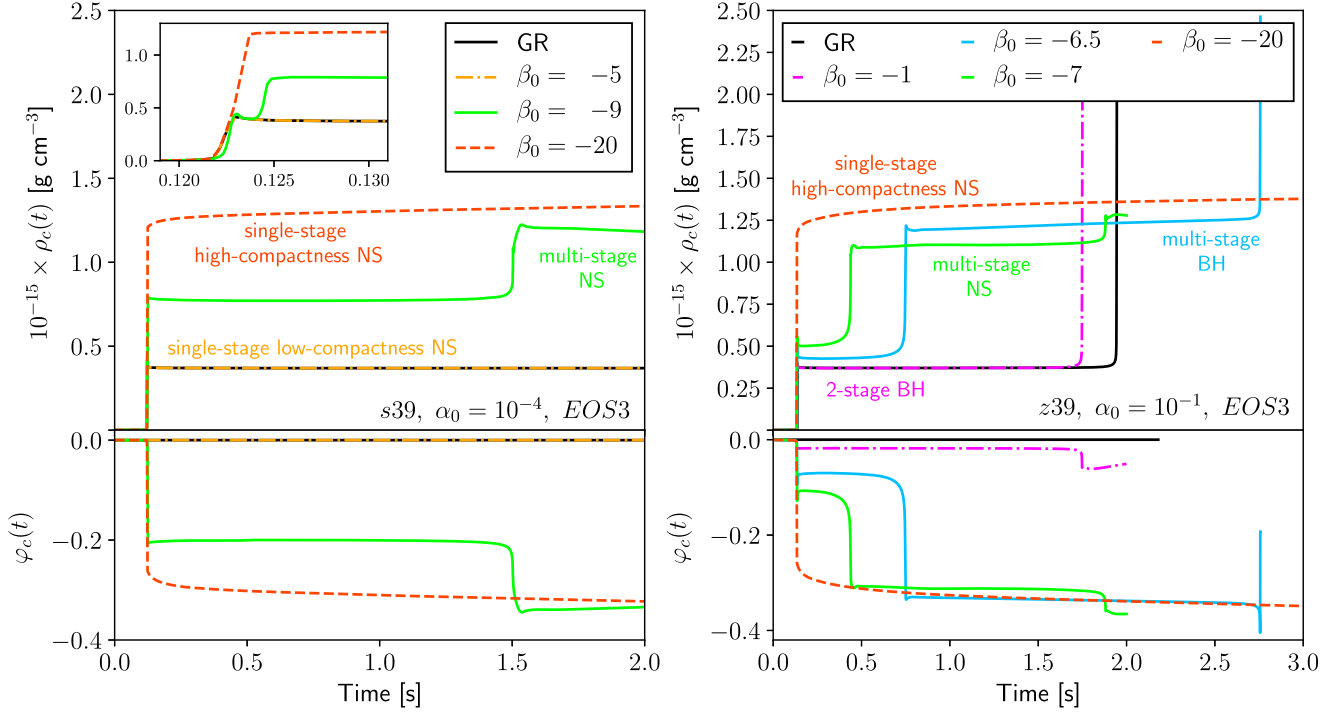
FIG. 1.   The central density (top panel) and maximal scalarization (bottom panel) are shown for representative examples of the five collapse configurations summarized in Sec. IV A. On the left, we show three evolutions of progenitor s39 with EOS3 for different ST parameters corresponding to the NS formation scenarios 1 (single-stage low-compactness NS), 4 (multistage NS), and 5 (single-stage high-compactness NS), respectively. On the right, we show the evolution of progenitor z39 with EOS3 for different ST parameters corresponding to scenarios 2 (two-stage BH formation), 3 (multistage BH formation), 4 (multistage NS), and 5 (single-stage high-compactness NS), respectively. For comparison, we display with solid black curves the corresponding evolution of the progenitors in GR which result in a NS in the left "s39" case and a BH in the right "z39" case. All curves have been obtained for a scalar mass $\mu = 10^{-14}$ eV.

to provide a remarkably comprehensive description of core collapse in massive ST gravity.

For this purpose, we first consider the possible end products of our collapse simulations. There are only three qualitatively different end states we have obtained in all of our simulations: (i) A weakly scalarized neutron star where $\varphi = \mathcal{O}(\alpha_0)$, (ii) a strongly scalarized neutron star with $\varphi = \mathcal{O}(1)$, or (iii) a black hole. The latter two end states, however, may be reached either directly or through several stages. This observation leads to our main classification scheme of five qualitatively different collapse scenarios.

(1) Single-stage collapse to a weakly scalarized neutron star.

(2) Two-stage formation of a black hole. Here the configuration temporarily settles down into a weakly scalarized neutron star. As the continued accretion of matter exceeds a threshold mass, the star undergoes a second collapse phase into a BH.

(3) Formation of a black hole through multiple stages. Here the configuration undergoes at least two approximately stationary neutron star phases; the first is weakly scalarized, and later phases are strongly scalarized.

(4) Collapse to a strongly scalarized neutron star through multiple stages. Here the configuration

intermittently forms one or more approximately stationary neutron star stages with ever increasing central density. The transition from weak to strong scalarization always occurs in the second collapse phase.

(5) Single-stage collapse to a strongly scalarized neutron star.

These five different scenarios are most conveniently visualized in terms of the central baryon density ρ_c and the central value of the scalar field φ_c as functions of time. We plot these quantities for a set of representative configurations in Fig. 1. A more detailed discussion of the five scenarios is given in Appendix A and a diagram-style visualization in Fig. 2.

The strength of the GW signal depends on the maximum scalarization achieved during the time evolution. This is not necessarily the degree of scalarization at the end of the simulation since black holes will descalarize in agreement with the no-hair theorems for BHs [63,64]. For[1] $\alpha_0 \ll 1$, this implies that case (1) always leads to a negligible GW

---

[1]For $\alpha_0 = \mathcal{O}(1)$ the scalar field will always reach a large amplitude $\varphi_{max} = \mathcal{O}(\alpha) = \mathcal{O}(1)$ and the distinction between weak and strong scalarization disappears. We only consider $\alpha_0 \leq 0.1$.
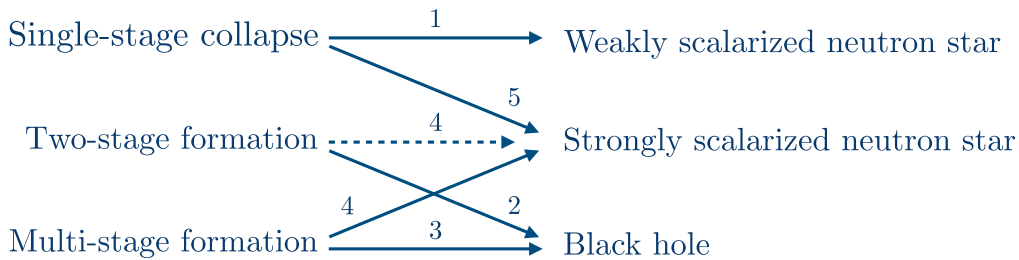
FIG. 2. A graphical illustration of the main collapse scenarios identified in our simulations. All stellar progenitors collapse into a weakly scalarized (GR-like) NS, a strongly scalarized NS, or a BH. As indicated in the diagram the outcomes may be reached promptly or in two or more stages. The two-stage formation of a strongly scalarized NS has been marked by a dashed arrow because this case appears in our set of simulations only a handful of times, and we suspect numerical noise to have impeded the occurrence of new stages. In the multistage NS category we count the simulations where all stages remain distinct, even if they happen on a short timescale.

signal, whereas cases (3), (4), and (5) always lead to strong signals. For the two-stage BH formation of case (2), we find that either weak or strong gravitational radiation is possible, depending on the degree of scalarization that can be achieved during the rapid collapse from a weakly scalarized neutron star to a BH. This sensitively depends on the parameters of the configuration.

In summary, for any given set of parameters, the collapse proceeds according to one of the five scenarios listed above. The question that remains is to establish a mapping between the parameter space and the possible outcomes. For this purpose we separate the parameters into two sets. The first consists of the EOS and progenitor parameters $(M_{\mathrm{ZAMS}}, Z, \Gamma_1, \Gamma_2, \Gamma_{\mathrm{th}})$ and the second of the ST parameters (α_0, β_0, μ). Let us then consider a given stellar progenitor with fixed ZAMS mass, metallicity, and EOS and consider the fate of this progenitor as a function of the ST parameters. Our first observation, which will be discussed in further detail below in Sec. V D, is that over a wide range of values the scalar mass μ does not affect the outcome qualitatively, but merely rescales the frequency of the GW signal and modifies its amplitude by a factor of order unity. In the remainder of this section, we set $\mu = 10^{-14}$ eV.

This leaves α_0 and β_0, and we now explore the main properties of the collapse scenarios in the plane spanned by these two parameters.

The resulting pattern is best understood by considering two examples, the progenitors s39 and z39 for EOS3 of Table I. These stellar models differ in their metallicity which leads to a different compactness of the core at bounce and, hence, significantly different collapse scenarios as shown in Fig. 3. In this figure, we display the maximal scalarization defined as

$$\varphi_{\mathrm{max}} = \max(|\varphi_c(t)|). \tag{34}$$

In all of our simulations, the extremal value of the central φ_c is negative, hence the modulus sign in Eq. (18).

[The overall sign of φ is merely a matter of convention; inspection of the action in Eq. (4) reveals that it is invariant under the simultaneous redefinitions $\varphi \to -\varphi$ and $\alpha_0 \to -\alpha_0$.] In the top row of Fig. 3, we plot φ_{max}, in logarithmic measure, as a function of β_0 for selected values α_0, and in the middle row it is shown in the form of a heat map in the (α_0, β_0) plane. Note that $\varphi_{\mathrm{max}} \propto \alpha_0$ for weakly scalarized configurations, whereas all strongly scalarized stars reach a comparable $\varphi_{\mathrm{max}} = \mathcal{O}(1)$. The measure φ_{max} furthermore determines the strength of the GW signal emitted in the collapse; $\varphi_{\mathrm{max}} = \mathcal{O}(1)$ always implies a strong GW signal and $\varphi_{\mathrm{max}} = \mathcal{O}(\alpha_0)$ a correspondingly weaker one by a factor $\alpha_0 \ll 1$. Finally, we display in the bottom row of Fig. 3 in the form of an (arbitrarily chosen) color code which of the above five collapse scenarios is realized for the s39 or z39 progenitor for ST parameters (α_0, β_0). Clearly, the two progenitors result in qualitatively different color maps. All our simulations of progenitor s39 result in a neutron star: for mildly negative β_0, a weakly scalarized NS is formed in a single stage. For moderate β_0, a multistage collapse leads to a strongly scalarized NS and for highly negative β_0 a strongly scalarized NS forms without intermediate stages. In contrast, we encounter for progenitor z39 the following scenarios as β_0 becomes more negative: two-stage BH formation, multistage BH formation, multistage formation of a strongly scalarized NS, single-stage formation of a strongly scalarized NS. The parameter α_0 only weakly affects the respective threshold values of β_0.

In principle, we could now construct heat maps analogous to those in Fig. 3 for any possible progenitor, i.e., for every mass M_{ZAMS}, metallicity Z, and EOS. We have done this for about 20 additional cases and always obtained a set of maps qualitatively equal to either the left neutron star case of Fig. 3 or the right black hole case in the figure. The boundaries of the different regions vary with EOS, M_{ZAMS}, and Z, but we always get one of the two maps. In consequence, the question which of the two qualitatively different maps of Fig. 3, the neutron-star or the black-hole
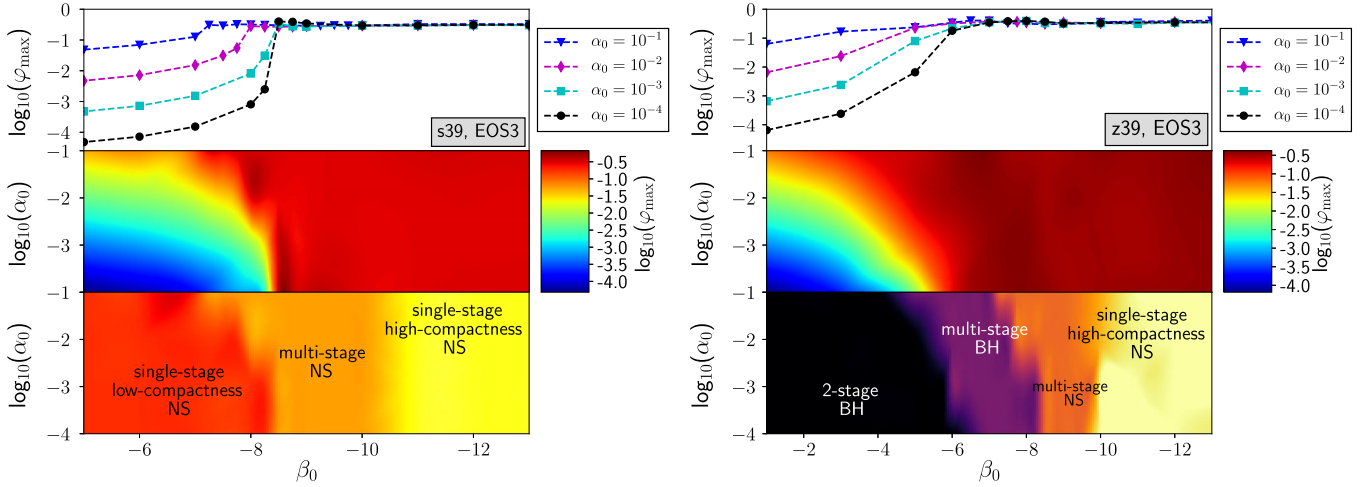
FIG. 3. We consider a fixed progenitor star with ZAMS mass 39 $M_\odot$, equation of state EOS3 of Table I, and fix the scalar mass at $\mu = 10^{-14}$ eV. The progenitor s39 in the left panel has solar metallicity $Z_\odot$, and the progenitor z39 in the right panel has primordial metallicity. Top row: For selected values of α_0, we plot the maximal scalarization of the collapsing star as a function of β_0. The middle row provides a color (or "heat") map of the same quantity in the (α_0, β_0) plane: "Red" = strong scalarization, "Blue" = weak scalarization. The bottom row presents a color code of the five qualitatively different collapse scenarios listed in Sec. IV A. Note that the s39 progenitor exclusively collapses to a neutron star, whereas u39 collapses to a black hole for $\beta_0 \gtrsim -8$ and to a neutron star for $\beta_0 \lesssim -8$. We find that every progenitor model results in heat maps in the (α_0, β_0) plane qualitatively equal to that on the left (the "neutron star" case) or that on the right (the "black hole" case).

case, applies to a given progenitor (and EOS) is completely determined by its fate in GR.

B. Dependency on the equation of state and progenitor model

The classification of the collapse scenarios has given us a qualitative picture of the possible outcomes of a stellar core collapse in ST gravity. The main task that remains is to understand more quantitatively how the boundaries in the diagrams of Fig. 3 depend on the choice of the EOS and the progenitor. Here we are particularly interested in the strength of the GW signal and will therefore focus on the sharp transition between weakly scalarized (blue) and the strongly scalarized (red) regions in the central panels in Fig. 3. Our strategy for this purpose is as follows. We consider EOS3 and EOSa from Table I as representative examples of a soft and a stiff EOS, respectively. Next, we note in Fig. 3 that the parameter α_0 only mildly affects whether a configuration is weakly or strongly scalarized; the corresponding β_0 threshold in the center panels of the figure varies by a few units but no more. Bearing in mind this variation, we fix in our analysis $\alpha_0 = 10^{-2}$.

We then have six combinations with different EOS and/or metallicity of the progenitor. For each of these cases we plot in Fig. 4 the maximum scalarization $\varphi_{\max}$ as a function of the progenitor mass M_{ZAMS} for selected values of β_0; these β_0 values have been chosen such that they bracket the threshold between weak and strong scalarization. The results of the figure are summarized as follows.

(i) The transition between weak and strong scalarization is abrupt, occurring in a brief interval around a threshold value β_0^*. Without fine-tuning β_0, we obtain either weakly or strongly scalarized configurations but rarely cases in between.

(ii) For β_0 values close to the threshold, the degree of scalarization can be highly sensitive to the ZAMS mass. Such a sensitive dependence on the parameters is reminiscent of the critical phenomena well known in gravitational collapse [65] and is also expected from the phase-transition character of the spontaneous scalarization phenomenon [2].

(iii) Besides this sensitive dependency near the critical β_0^*, the only significant variation of the degree of scalarization with the ZAMS mass occurs at the onset of BH formation in the center-right and bottom-right panels of Fig. 4. Here the scalarization increases visibly at $M_{\mathrm{ZAMS}} \approx 30\ M_\odot$ and $35\ M_\odot$, respectively. Progenitor masses below the threshold value result in weakly scalarized NSs and higher masses lead to BH formation and stronger scalarization. Note, however, the logarithmic scaling of the vertical axis, so that even in these cases, the strong variation of φ_c with M_{ZAMS} is restricted to β_0 values close to the critical threshold β_0^*.

(iv) For β_0 values significantly below or above the threshold, our simulations show only a mild dependence of the scalarization on the progenitor mass M_{ZAMS}. The same holds for the metallicity Z.

(v) Stiff EOSs result in less compact neutron stars and correspondingly more negative threshold values β_0^* for strong scalarization. For soft EOSs, highly compact neutron stars can form even for mild β_0 values and lead to strong scalarization.
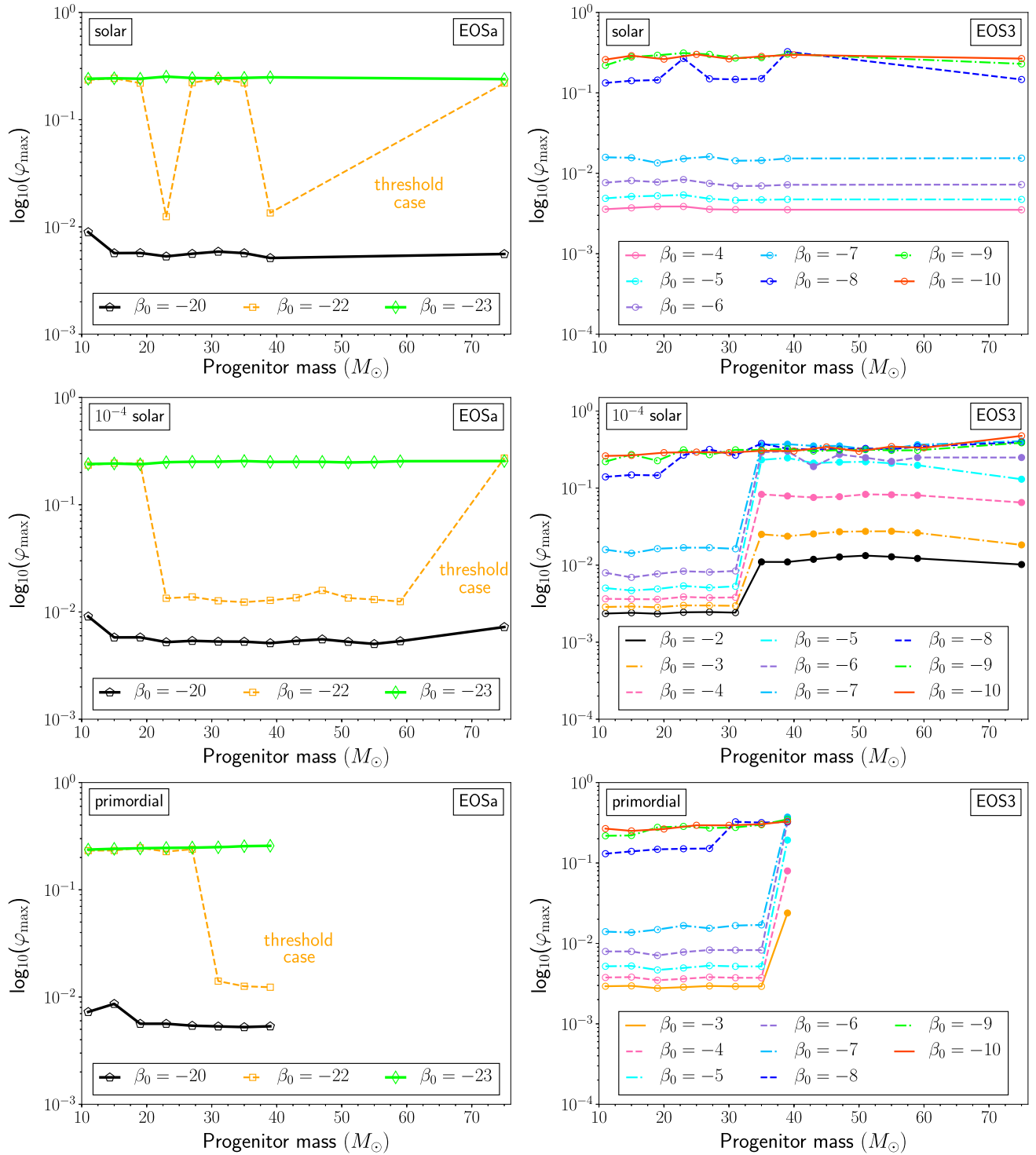
FIG. 4. Each panel shows the maximum scalarization of a core collapse as a function of the ZAMS progenitor mass for selected values of β_0 that bracket the transition from weak to strong scalarization. The left column represents EOSa and the right column EOS3. The rows represent a different metallicity as labeled in the panels. The right panels and the top-left panel exclusively contain collapse scenarios forming NSs. In the center-right and bottom-right panels, we distinguish NS cases from those forming BHs by using empty or filled symbols, respectively. Note that for primordial metallicity, the catalog of stellar progenitors contains models up to $M_{\mathrm{ZAMS}} = 40 \, M_\odot$ only.

In summary, we observe strong scalarization when β_0 becomes more negative than a threshold value β_0^*. This threshold is ≈ -25 for a stiff EOS but drops to the well-known limit $\beta_{0,\mathrm{thr}} - 4.35$ observed for the spontaneous scalarization of stationary neutron-star models in massless ST theory [2,32]. This threshold varies only mildly with the mass or the metallicity of the progenitor model.

Throughout this analysis, we set the scalar mass parameter $\mu = 10^{-14}$ eV. As it turns out, the degree of scalarization barely changes even when we vary μ over several orders of magnitude. This insensitivity to μ of the strong scalarization effect is not only supported by our simulations, but can also be understood at the analytic level. This will be done in the next section where we also discuss in more detail the propagation of the wave signal to astrophysically large distances.

V. WAVE EXTRACTION AND PROPAGATION

sec:wave_extraction_and_propagation In this section, the extraction of the scalar field from the core collapse simulations is described along with a procedure for converting this into a prediction for the GW signal at astrophysically large distances, potentially observable by LIGO/Virgo. The latter step is complicated by the dispersive nature of wave propagation for massive fields; it will be shown how this dispersion generically leads to the *inverse chirp* described in [37].

There are two natural length scales relevant to the problem: the gravitational radius associated with the mass of the remnant NS, $r_G = GM_{\mathrm{NS}}c^{-2}$; and the reduced Compton wavelength for the massive scalar field, $\lambdabar_C = c/\omega_*$ where $\omega_* = \mu c^2 \hbar^{-1}$. The remainder of this section again uses natural units in which $G = c = 1$.

At large distances from the star ($r \gg r_G$) the dynamics of the gravitational scalar are, to a good approximation, governed by the flat-space Klein-Gordon equation,

$$\partial_t^2 \varphi - \nabla^2 \varphi + \omega_*^2 \varphi = 0. \tag{35}$$

In spherical symmetry (using coordinates $\{t, r, \theta, \phi\}$) the field depends only on time and radius [$\psi = \psi(t; r)$], the Laplacian is given by $\nabla^2 \cdot = r^{-2}\partial_r(r^2\partial_r \cdot)$, and the rescaled field $\sigma \equiv r\varphi$ satisfies a 1D wave equation,

$$\partial_t^2 \sigma - \partial_r^2 \sigma + \omega_*^2 \sigma = 0. \tag{36}$$

Consider first the behavior of a single Fourier mode, $\sigma \propto e^{-i(\omega t - kr)}$; Eq. (36) gives the *dispersion relation*

$$\omega^2 = k^2 + \omega_*^2. \tag{37}$$

The wave number, k, is real for high frequencies ($|\omega| > \omega_*$) and the solution describes a propagating wave. For low frequencies ($|\omega| < \omega_*$; including the static case $\omega = 0$) the wave number is imaginary leading to solutions which

decay exponentially over a characteristic length $\lambdabar_C$. The critical frequency ω_* associated with the scalar field mass acts as a low frequency cutoff in the GW spectrum. For propagating solutions, the phase velocity ($v_{\mathrm{phase}} = \omega/k = [1 - (\omega_*/\omega)^2]^{-1/2}$) is superluminal, while the group velocity ($v_{\mathrm{group}} = d\omega/dk = [1 - (\omega_*/\omega)]^{+1/2}$) is subluminal.

In the massless case ($\omega_* = 0$), the general solution to Eq. (36) can be written as the sum of ingoing and outgoing pulses traveling at the speed of light. This makes interpreting the output of core collapse simulations particularly simple. First, one extracts the field as a function of time at a fixed *extraction radius*, $\sigma(t; r_{\mathrm{ex}})$. This radius must be sufficiently large that (i) the flat space Eq. (35) holds, and (ii) r_{ex} is in the wave zone so that the signal has decoupled from the source and is purely outgoing. In the massless case both (i) and (ii) are satisfied by choosing $r_{\mathrm{ex}} \gg r_G$. Then, the signal as a function of time at some larger *target radius*, $\sigma(t; r)$, is simply obtained via $\sigma(t - [r - r_{\mathrm{ex}}]; r) = \sigma(t; r_{\mathrm{ex}})$. The only change in the signal between r_{ex} and r is a time delay and a reduction in the amplitude of the field φ by a factor (r/r_{ex}).

We seek an analogous method in the massive case ($\omega_* > 0$) for relating the signal at the extraction radius to the signal at the much larger target radius. The extraction radius is chosen to satisfy the two conditions as before, but now (ii) requires $r_{\mathrm{ex}} \gg \lambdabar_C$. This is generally a stricter condition than $r_{\mathrm{ex}} \gg r_G$; for $\mu = 10^{-14}$ eV the Compton wavelength is $\lambdabar_C \approx 10^7$ m, whereas the gravitational radius for NSs is typically only $r_G \sim 10^3$ m. In this paper the extraction radius is taken to be $r_{\mathrm{ex}} = 7.0 \times 10^7$ m. The target radius, the distance of the supernova from Earth, is very much larger, e.g., $\sim$10 kpc.

The remainder of this section describes two methods for evolving signals from the extraction radius out to large radii. First, a numerical evolution of Eq. (36) in the time domain is described. This numerical method, while very accurate at short distance, is of limited use in practice because it struggles to cope with the very large astrophysical distances. Second, an analytic method for solving Eq. (36) in the frequency domain is described. The two methods are validated by comparing them against each other in the regime where both can be evaluated. Finally, the analytic method is used to study the asymptotic behavior at large distances using the stationary phase approximation (SPA).

A. Numerical evolution in the time domain

Given suitable initial data it is possible to numerically evolve Eq. (36). Here it is necessary to evolve some given outgoing data on a timelike surface out to larger radii (see Fig. 5). Equation (36) is written in a manner that makes a $1 + 1$ dimensional split obvious using the coordinates $\{t, r\}$. However, these coordinates are not well adapted for signals traveling at, or near, the speed of light.
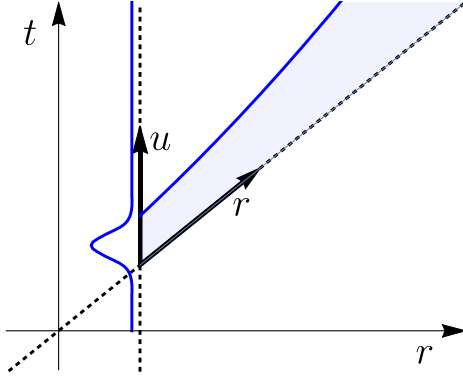
FIG. 5. A sketch of the coordinates used in the numerical evolution. The main axes show the standard $\{t, r\}$ coordinates and the inset arrows show the $\{u, r\}$ coordinates. The vertical blue line indicates the signal as a function of time at the extraction radius, $\sigma(t; r_{\text{ex}})$, and the shading indicates the region where the signal propagates dispersively. A numerical grid based on the $\{u, r\}$ coordinates can cover the shaded region with less redundant space than one based on $\{t, r\}$.

Alternatively, and much more efficiently, a $1 + 1$ split can be implemented based on coordinates $\{u, r\}$, where $u \equiv t - r$ is the (null) retarded time coordinate. Using these coordinates the wave equation becomes

$$2\partial_u \partial_r \sigma - \partial_r^2 \sigma + \omega_*^2 \sigma = 0. \quad (38)$$

By defining the conjugate momentum $\Pi_u \equiv \partial_u \sigma(u; r)$, Eq. (38) can be reduced down to the first order form.

Given an initial signal on the extraction sphere, $\sigma(u; r_{\text{ex}})$, it is straightforward to solve Eq. (38) using standard techniques; in our case a *method of line* integration with the *iterated Crank-Nicholson* scheme [66]. From this numerical solution, we directly extract the signal at some larger target radius, $\sigma(u; r)$.

B. Analytic evolution in the Fourier domain

We now revert to coordinates $\{t, r\}$ in Eq. (36). With the Fourier transform conventions

$$\tilde{\sigma}(\omega; r) = \int_{-\infty}^{\infty} \mathrm{d}t \sigma(t, r) e^{i\omega t}, \quad (39)$$

$$\sigma(t; r) = \int_{-\infty}^{\infty} \frac{\mathrm{d}\omega}{2\pi} \tilde{\sigma}(\omega, r) e^{-i\omega t}, \quad (40)$$

the Fourier transform of Eq. (36) yields the simple harmonic motion equation for $\tilde{\sigma}(\omega; r)$,

$$\partial_r^2 \tilde{\sigma}(\omega; r) = -(\omega^2 - \omega_*^2)\tilde{\sigma}(\omega; r). \quad (41)$$

Defining $k^+ \equiv +\sqrt{\omega^2 - \omega_*^2}$ as the positive root of the dispersion relation in Eq. (37), the solution to Eq. (41) can be written in terms of two arbitrary functions,

$$\tilde{\sigma}(\omega; r) = f(\omega)e^{ik^+(r - r_{\text{ex}})} + g(\omega)e^{-ik^+(r - r_{\text{ex}})}. \quad (42)$$

The radial coordinate has been shifted to the extraction radius for later convenience. Taking the inverse Fourier transform to convert back into the time domain gives

$$\sigma(t; r) = \int_{-\infty}^{\infty} \frac{\mathrm{d}\omega}{2\pi} [f(\omega)e^{ik^+(r - r_{\text{ex}})} \\ + g(\omega)e^{-ik^+(r - r_{\text{ex}})}]e^{-i\omega t}. \quad (43)$$

The fact that the field φ is real imposes some constraints on the otherwise arbitrary functions f and g:

(a) $\sigma(t; r) \in \mathbb{R} \Rightarrow \tilde{\sigma}(\omega; r) = \tilde{\sigma}^*(-\omega; r) \Rightarrow$

$$\begin{cases} f(\omega) = g^*(-\omega) & \text{if } |\omega| > \omega_* \\ f(\omega) = f^*(-\omega) \quad \text{and} \quad g(\omega) = g^*(-\omega) & \text{if } |\omega| < \omega_* \end{cases}. \quad (44)$$

A further constraint on the function g is obtained by imposing boundary conditions at infinity. The field φ must decay as $1/r$ (or faster) which implies that $\tilde{\sigma}(\omega; r)$ remains bounded at large radii. From Eq. (43), and recalling that k^+ is imaginary for $|\omega| < \omega_*$, gives the constraint

(b) $g(\omega) = 0 \quad \text{if } |\omega| < \omega_*. \quad (45)$

The constraints (a) and (b) can be used to eliminate $g(\omega)$ in favor of $f(\omega)$. Furthermore, the symmetries implied by the constraint (a) allow the Fourier integral in Eq. (43) to be written over positive frequencies; the general solution in Eq. (43) now becomes

$$\sigma(t; r) = 2\Re \left\{ \int_0^{\omega_*} \frac{\mathrm{d}\omega}{2\pi} f(\omega)e^{ik^+(r - r_{\text{ex}})} e^{-i\omega t} \right. \\ \left. + \int_{\omega_*}^{\infty} \frac{\mathrm{d}\omega}{2\pi} [f(\omega)e^{ik^+(r - r_{\text{ex}})} + f^*(-\omega)e^{-ik^+(r - r_{\text{ex}})}]e^{-i\omega t} \right\}. \quad (46)$$

From Eq. (46), and considering the sign of k^+, it can be seen that the high frequencies $f(\omega > \omega_*)$ represent outgoing modes, the large negative frequencies $f(\omega < -\omega_*)$ represent ingoing modes, and the intermediate frequencies $f(|\omega| < \omega_*)$ represent nonpropagating modes.

It only remains to relate the unknown function $f(\omega)$ to the (purely outgoing) scalar profile at the extraction radius obtained from the core collapse simulation, $\sigma(t; r_{\text{ex}})$. The function $f(\omega)$ is given by

$$f(\omega) = \begin{cases} 0 & \text{if } \omega \leq -\omega_* \\ \tilde{\sigma}(\omega; r_{\text{ex}}) & \text{if } \omega > -\omega_* \end{cases}. \quad (47)$$

Substituting into Eq. (46), and returning to writing the integral over both positive and negative frequencies, gives

$$\sigma(t;r) = \int \frac{d\omega}{2\pi} \tilde{\sigma}(\omega; r_{\text{ex}})$$

$$\times \left\{ \begin{array}{l} e^{-ik^+(r-r_{\text{ex}})} \text{ if } \omega \leq -\omega_* \\ e^{+ik^+(r-r_{\text{ex}})} \text{ if } \omega > -\omega_* \end{array} \right\} e^{-i\omega t}. \quad (48)$$

This shows that the frequency domain signal at the target radius is related to that at the extraction radius via

$$\tilde{\sigma}(\omega; r) = \tilde{\sigma}(\omega; r_{\text{ex}}) \times \left\{ \begin{array}{l} e^{-ik^+(r-r_{\text{ex}})} \text{ if } \omega \leq -\omega_* \\ e^{+ik^+(r-r_{\text{ex}})} \text{ if } \omega > -\omega_* \end{array} \right\}. \quad (49)$$

Note that the effect of the dispersion enters only in the complex phase of the Fourier transform. Therefore, the effect of the dispersion is to disperse the signal, rearranging the frequency components in time, while leaving the overall power spectrum invariant for all $|\omega| > \omega_*$. Lower frequencies, $|\omega| < \omega_*$, are exponentially suppressed during propagation and are not observable at large distances.

We now have a prescription for analytically propagating signals out to larger radii. First, numerically evaluate the fast Fourier transform of the scalar profile on the extraction sphere, $\tilde{\sigma}(\omega; r_{\text{ex}})$. Second, use Eq. (49) to obtain the Fourier domain signal at the target radius, $\tilde{\sigma}(\omega; r)$. Finally, numerically evaluate the inverse Fourier transform to obtain the desired signal, $\sigma(t; r)$. In Appendix C we compare the results of analytically propagating signals in this way with the results obtained via numerical evolution described in Sec. V A and find good agreement.

Unfortunately, neither of the methods described (in their current form) is suitable for propagating the signal to astrophysically large distances (e.g., $r_{\text{ex}} = 10$ kpc). The unavoidable problem is that as the signal propagates further, the longer (i.e., containing more cycles) it becomes due to the dispersive stretching. This poses two problems for the time domain numerical integration: first, the evolution becomes increasingly expensive due to the large numerical grids required; and second, the numerical errors tend to grow as the signal is propagated over greater distances. The analytic frequency domain method can be pushed to somewhat larger radii; however, even this fails when the signal eventually becomes longer than the largest array for which the fast Fourier transform can be numerically evaluated. The next section describes how the behavior of the scalar field at very large distances may be studied.

C. Asymptotic behavior: The inverse chirp

As the signal is stretched out, it becomes ever more oscillatory, and the amplitude varies more slowly relative to the phase. Therefore, in the large distance limit the stationary phase approximation may be used to evaluate the inverse Fourier transform in Eq. (48). It should be noted that the SPA *becomes* valid at large radii regardless of whether it was initially valid for the signal at the extraction

radius. As will be shown below, dispersive signals tend to "forget" the details of their initial profile as they propagate over large distances and always tend to a generic "inverse chirp" profile.

The initial Fourier domain signal on the extraction sphere may be decomposed into its amplitude and phase:

$$\tilde{\sigma}(\omega; r_{\text{ex}}) = \mathcal{A}(\omega; r_{\text{ex}}) e^{i\Psi(\omega)}. \quad (50)$$

As noted above, at large radii frequencies $|\omega| < \omega_*$ do not contribute to the signal because they decay exponentially with r. It will be convenient to write the time domain solution at large radii in Eq. (48) as an integral over positive frequencies only:

$$\sigma(t; r) = 2\Re \left\{ \int_{\omega_*}^{\infty} \frac{d\omega}{2\pi} \mathcal{A}(\omega) e^{i\psi(\omega, t)} \right\}, \quad (51)$$

where the modified complex phase is defined as $\psi(\omega, t) \equiv \Psi(\omega) + k^+(r - r_{\text{ex}}) - \omega t$. This phase has a stationary point when $\partial \psi(\omega, t)/\partial \omega = 0$ which is satisfied by

$$t = \frac{d\Psi(\omega)}{d\omega} + \frac{\omega(r - r_{\text{ex}})}{\sqrt{\omega^2 - \omega_*^2}}. \quad (52)$$

Note that the final term in Eq. (52) can be written as $(r - r_{\text{ex}})/v_{\text{group}}$. In the limit $r \gg r_{\text{ex}}$ the final term in Eq. (52) becomes dominant and the $d\Psi/d\omega$ term can be neglected. In this approximation, it is straightforward to invert Eq. (52), which gives us the frequency of the signal at r as a function of time, $\omega = \Omega(t)$, where

$$\Omega(t) = \frac{\omega_* t}{\sqrt{t^2 - (r - r_{\text{ex}})^2}}, \quad \text{for } t > r - r_{\text{ex}}. \quad (53)$$

This frequency varies as an *inverse chirp* (see Fig. 6) with low frequencies arriving after high frequencies. The origin of the inverse chirp is easily understood as the modes of each frequency arriving at a time corresponding to the group velocity of that frequency.

All that remains is to evaluate the amplitude as a function of time. This can also be done via the SPA. The integrand in Eq. (51) is highly oscillatory when $r - r_{\text{ex}}$ is large, except for frequencies near $\Omega(t)$ which therefore dominate the result. Expanding the amplitude to zeroth order, and the phase to quadratic order, about $\omega = \Omega(t)$ and substituting into Eq. (51) gives

$$\sigma(t; r) = 2\Re \left\{ \mathcal{A}[\Omega] e^{i\psi(\Omega, t)} \int_{\omega_*}^{\infty} \frac{d\omega}{2\pi} e^{\frac{i}{2}(\omega - \Omega)^2 \psi''} \right\}, \quad (54)$$

where $\psi'' \equiv \partial^2 \psi/\partial \omega^2 |_{\omega = \Omega}$. The integrand in Eq. (54) is dominated by frequencies near $\omega = \Omega$; at the current approximation order, the integration limits can be changed

to $\int_{\Omega-a}^{\Omega+b} d\omega$ for any $a, b > 0$. Choosing $a, b \to \infty$, and changing variables to $u^2 = (\omega - \Omega)\psi''$ gives

$$\sigma(t; r) = \Re\left\{\frac{\mathcal{A}(\Omega)e^{i\psi(\Omega, t)}}{\sqrt{\pi^2|\psi''|}}\int_{-\infty}^{\infty} du\, e^{\frac{i}{2}u^2 \text{sign}(\psi'')}\right\}. \quad (55)$$

The integral in Eq. (55) is a standard Gaussian integral which may be readily evaluated to give

$$\sigma(t; r) = \Re\{A(t; r)e^{i\phi(t; r)}\}, \quad (56)$$

where the amplitude and phase are given by

$$A(t; r) = \sqrt{\frac{2[\Omega^2 - \omega_*^2]^{3/2}}{\pi\omega_*^2(r - r_{\text{ex}})}}\mathcal{A}(\Omega), \quad (57)$$

$$\phi(t; r) = \Psi(\Omega) + \sqrt{\Omega^2 - \omega_*^2}(r - r_{\text{ex}}) - \Omega t - \frac{\pi}{4}, \quad (58)$$

where $\Omega(t)$ is given in Eq. (53) [cf. Eq. (11) in [37]]. At each instant the signal is quasimonochromatic with a frequency $\Omega(t)$ and an amplitude, $A(t; r)$, proportional to the square root of the power spectrum of the initial (extraction radius) signal evaluated at that frequency divided by a factor to account for the dispersive stretching of the signal.

The inverse chirp profile described by Eq. (58) (see Fig. 6) is an extremely robust prediction for the signal observed at large distances. The signal frequency as a function of time depends only on the distance to the source and the mass of the scalar field (and there is a near universal scaling behavior with the scalar mass, as described in the next section). The frequency as a function of time is completely independent of the details of the original signal near the source. The signal amplitude as a function of time
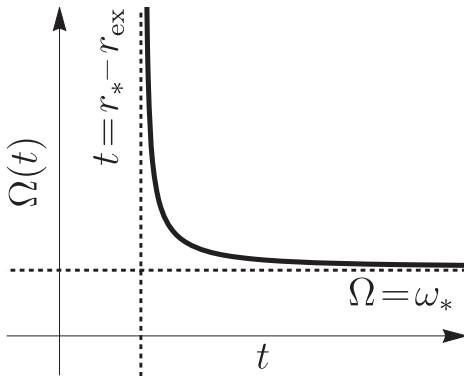
FIG. 6. A sketch plot showing the time-frequency structure of the "inverse chirp" in Eq. (53). The frequency decays over time; the high frequency components (traveling at almost the speed of light) arrive first, followed by the slower low frequency components. Frequencies below ω_* are exponentially suppressed and never reach large radii.

does retain some information about the original source, through its dependence on the spectrum $\mathcal{A}(\omega)$, although even this gets highly smeared out by the dispersion. The inverse chirp waveforms can be extremely long and highly oscillatory; for the scalar field masses and distances of interest here (i.e., $\mu \approx 10^{-14}$ eV and $r_{\text{ex}} \approx 10$ kpc) the signals can retain frequencies and amplitudes potentially detectable by LIGO/Virgo for centuries. These signals are best visualized by plotting the amplitude and frequency separately as functions of time (see Fig. 2 and the accompanying discussion in [37]).

D. Approximate universality under changes of the scalar mass

1. Theoretical considerations

The asymptotic behavior of the wave signal under its dispersive propagation is determined by Eq. (53) for the frequency and Eq. (57) for the amplitude of the signal. The dependence of the propagated signal on the scalar mass μ through its associated frequency ω_* becomes clearer if we rewrite the solution in terms of dimensionless quantities. For this purpose, we define the rescaled frequency, radius, and time by

$$\bar{\Omega} = \frac{\Omega}{\omega_*}, \qquad \bar{r}_{\text{ex}} = \omega_* r_{\text{ex}},$$
$$\bar{t} = \omega_* t, \qquad \bar{r} = \omega_* r. \quad (59)$$

In this notation, Eqs. (53), (58), and (57) become

$$\bar{\Omega}(\bar{t}, \bar{r}) = \frac{\bar{t}}{\sqrt{\bar{t}^2 - (\bar{r} - \bar{r}_{\text{ex}})^2}},$$

$$\phi(\bar{t}, \bar{r}) = \sqrt{\bar{\Omega}^2 - 1}(\bar{r} - \bar{r}_{\text{ex}}) - \bar{\Omega}\bar{t} - \frac{\pi}{4} + \text{Arg}[\tilde{\sigma}(\Omega; r_{\text{ex}})],$$

$$A(\bar{t}, \bar{r}) = \sqrt{\frac{2}{\pi}}\frac{\omega_*(\bar{\Omega}^2 - 1)^{3/4}}{(\bar{r} - \bar{r}_{\text{ex}})^{1/2}}\text{Abs}[\tilde{\sigma}(\Omega; r_{\text{ex}})]. \quad (60)$$

We have thus been able to absorb much of the dependence on the scalar mass in terms of a simple rescaling of radius, time, and frequency. But two issues remain: (i) a factor of ω_* is present in the amplitude $A(\bar{t}, \bar{r})$, and (ii) the phase and amplitude implicitly depend on the scalar mass through the phase and amplitude of the Fourier transform $\tilde{\sigma}(\Omega, r_{\text{ex}})$. Further progress requires information about the signal at r_{ex}. More specifically, we can exploit two features that we find to be satisfied approximately in the generation of scalar radiation in stellar collapse in ST theory.

The first observation is that the scalar field at the center of the star evolves largely independently of the scalar mass. Likewise, the scalar profile $\varphi(r)$ at late stages in the evolution is independent of the scalar mass (always assuming that the other parameters of the configuration are held fixed). This suggests that in the region of wave

generation $\sigma(t, r)$ [rather than $\sigma(\bar{t}, \bar{r})$] is approximately independent of the scalar mass. Let us take this as a working hypothesis and compute its implications.

From the definition of the Fourier transform we obtain

$$\tilde{\sigma}(\Omega; r_{\mathrm{ex}}) = \int_{-\infty}^{\infty} \sigma(t; r_{\mathrm{ex}}) e^{i\Omega t} dt$$
$$= \frac{1}{\omega_*} \int_{-\infty}^{\infty} \sigma(\bar{t}/\omega_*; r_{\mathrm{ex}}) e^{i\bar{\Omega}\bar{t}} d\bar{t}. \quad (61)$$

Now we employ the second empirical observation. Near the star, the dynamics in the scalar field are dominated by the sudden transition from weak (or zero) to strong scalarization. The time dependence of the scalar field at a given radius is therefore approximated by a Heaviside function, $\sigma(t, r_{\mathrm{ex}}) \sim f(r_{\mathrm{ex}}) H(t)$. The Heaviside function satisfies $H(t) = H(at)$ for a real constant a, and we can use $\sigma(\bar{t}/\omega_*; r_{\mathrm{ex}}) = \sigma(\bar{t}; r_{\mathrm{ex}})$ in Eq. (61), so that

$$\tilde{\sigma}(\Omega; r_{\mathrm{ex}}) = \frac{1}{\omega_*} \int_{-\infty}^{\infty} \sigma(\bar{t}; r_{\mathrm{ex}}) e^{i\bar{\Omega}\bar{t}} d\bar{t} = \frac{1}{\omega_*} \tilde{\sigma}(\bar{\Omega}; r_{\mathrm{ex}}). \quad (62)$$

We thus acquire a factor $1/\omega_*$ in the amplitude of $\tilde{\sigma}(\Omega; r_{\mathrm{ex}})$ and no change in its phase and Eq. (60) becomes

$$\bar{\Omega}(\bar{t}, \bar{r}) = \frac{\bar{t}}{\sqrt{\bar{t}^2 - (\bar{r} - \bar{r}_{\mathrm{ex}})^2}},$$
$$\phi(\bar{t}, \bar{r}) = \sqrt{\bar{\Omega}^2 - 1}(\bar{r} - \bar{r}_{\mathrm{ex}}) - \bar{\Omega}\bar{t} - \frac{\pi}{4} + \mathrm{Arg}[\tilde{\sigma}(\bar{\Omega}; r_{\mathrm{ex}})],$$
$$A(\bar{t}, \bar{r}) = \sqrt{\frac{2}{\pi}} \frac{(\bar{\Omega}^2 - 1)^{3/4}}{(\bar{r} - \bar{r}_{\mathrm{ex}})^{1/2}} \mathrm{Abs}[\tilde{\sigma}(\bar{\Omega}; r_{\mathrm{ex}})]. \quad (63)$$

This gives us a universal expression for the wave signal which depends on the scalar mass ω_* only through the rescaling of time, radius, and frequency according to Eq. (59). In other words, if we know the signal $[\Omega(t, r), \phi(t, r), A(t, r)]$ of a configuration with mass parameter $\omega_{*,1}$, we obtain the signal for the same configuration in ST theory with $\omega_{*,2}$ by replacing $t \to \lambda t$, $r \to \lambda r$, $\Omega \to \Omega/\lambda$, $(\phi, A) \to (\phi, A)$ with $\lambda = \omega_{*,1}/\omega_{*,2}$.

2. Results

The universality under changes in the scalar mass ω_* will only hold approximately for a number of reasons: (i) At least at small radii, the wave propagation will be governed by the field equations (18)–(22) rather than the Klein-Gordon equation underlying the calculations of this section. (ii) The time dependence of the scalar field near the source is only approximately of Heaviside shape. (iii) Especially for large scalar mass parameters, we expect the function $\sigma(t, r)$ no longer to be independent of the value ω_* as the Compton wavelength approaches the size of the stellar core. For example, a reduced Compton wavelength $\lambdabar_c < 100$ km corresponds to a scalar mass

$\mu > 1.97 \times 10^{-12}$ eV and frequency $\omega_* > 3000$ s^{-1}. (Note that such large values of the scalar mass are no longer ideal for tests with GW observations as the contributions relevant for LIGO-Virgo partially fall inside the exponentially suppressed regime $\omega < \omega_*$.)

So how well is the universality predicted by Eq. (63) satisfied in practice? To address this question we have numerically explored a range of configurations. For each of these, we have fixed α_0, β_0, the EOS, and the progenitor model and then performed a one-parameter study varying μ in the range 2×10^{-15} eV $\leq \mu \leq 10^{-12}$ eV. All of these cases exhibit the characteristic behavior we illustrate in Figs. 7 and 8 for the specific case of an s12 progenitor star, EOS5, and ST parameters $\alpha_0 = 10^{-2}$, $\beta_0 = -20$.

The wave amplitude σ in Fig. 7 has been extracted from the core collapse simulations at rescaled extraction radius $\bar{r}_{\mathrm{ex}} = 5.07 = (\mu/10^{-14} \text{ eV})^{-1} \times 10^5$ km. We have shifted the signals in time such that their peaks align at $\bar{t} = 0$. The main difference of the signals is a monotonic drop in amplitude as μ increases; the strongest signal (for $\mu = 2 \times 10^{-15}$ eV) exceeds the weakest one (for $\mu = 10^{-12}$ eV) by a factor of about 5. For scalar mass values $\mu < 2 \times 10^{-15}$ eV, simulations over several wave cycles become prohibitively costly (recall that the corresponding physical timescales $\propto 1/\mu$). We have, however, performed short simulations up to the first strong peak in the signal. This peak, shifted to $\bar{t} = 0$ in Fig. 7, corresponds to the core bounce at $t = \mathcal{O}(0.1)$ s and can be computed in shorter simulations lasting up to about $t \approx r_{\mathrm{ex}}$. We find the monotonic trend in the amplitude to continue with an
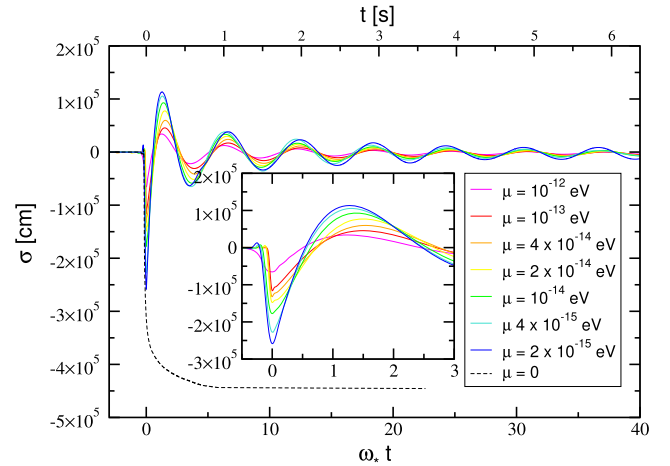

FIG. 7. GW signal $\sigma(t, r_{\mathrm{ex}})$ extracted from the collapse of an s12 (i.e., $12\,M_\odot$, solar metallicity) progenitor model with $\alpha_0 = 10^{-2}$, $\beta_0 = 20$, using EOS5 at $\omega_* r_{\mathrm{ex}} = 5.07$ for different values of the scalar mass $\mu \in [2 \times 10^{-15} \text{ eV}, 10^{-12} \text{ eV}]$. The overall amplitude increases monotonically with decreasing μ. For reference, we also show the wave signal obtained for $\mu = 0$ (dashed curve). In this case, we cannot rescale the time with ω_* and instead measure time in seconds as labeled on the upper horizontal axis.
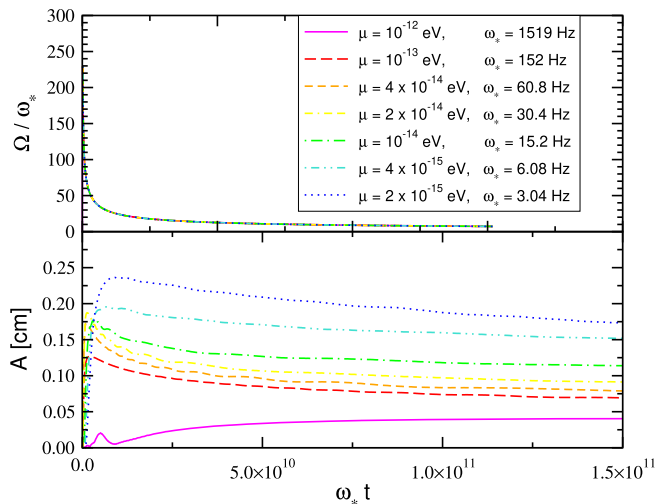
FIG. 8. The wave signals of Fig. 7 propagated according to Eqs. (53) and (57) to $\omega_* r = 1.56 \times 10^{13} = (\mu/10^{-14}\,\text{eV})^{-1} 10\,\text{kpc}$. As expected, the curves for the rescaled frequency Ω/ω_* overlap in the upper panel. The amplitude in the lower panel shows a mild increase as we decrease the scalar mass μ.

upper bound given by the limiting case $\mu = 0$. The wave signal $\sigma(t)$ resulting from this limit can no longer be rescaled according to Eq. (59) since $\omega_* = 0$; instead, we have included it in Fig. 7 (black dashed curve) as a function of physical time t denoted on the upper horizontal axis.

Amplitude and frequency of the corresponding waveforms propagated to $\omega_* r = 1.56 \times 10^{13} = (\mu/10^{-14}\,\text{eV})^{-1} 10$ kpc are shown in Fig. 8. We find the same monotonic increase of the wave amplitude as μ decreases from 10^{-12} eV to 2×10^{-15} eV with, again, an overall factor of about 5 between the extreme cases. We furthermore notice an additional reduction in the high-frequency contributions for $\mu = 10^{-12}$ eV which manifests itself in the reduced signal strength at early times in Fig. 8. As expected from Eq. (63), the rescaled frequencies $\bar{\Omega}(\bar{r})$ agree exactly. We have explored in the same way other configurations differing from this case in the ST or EOS parameters or the mass of the stellar progenitor model. All cases show the same behavior: the rescaled frequency is independent of the scalar mass μ when plotted as a function of rescaled time $\bar{t}$, whereas the amplitude shows a monotonic increase by an overall factor of about 5 as μ decreases from 2×10^{-15} eV to 10^{-12} eV.

Finally, we have explored whether the onset of strong scalarization as shown in the heat maps in Fig. 3 depends on the scalar mass μ. The answer is *no* for all configurations we have tested; while the degree of strong scalarization mildly weakens for larger μ, the transition occurs at the same β_0 independent of the value of μ.

In summary, once we have computed a wave signal from a configuration for some value of μ, the signal for the (otherwise) identical configuration with a different scalar mass $\hat{\mu}$ can be obtained by a linear rescaling of the argument and result of the frequency $\Omega(t)$ while an

approximate estimate of the amplitude $A(t)$ can be obtained by a rescaling of the time (but not of A). The frequency scaling is exact within the SPA, whereas the amplitude scaling is approximate to within an order of magnitude and we cannot rigorously exclude exceptions from its rule.

VI. GW OBSERVATIONS

Core collapse in massive scalar tensor gravity can lead to the emission of large quantities of scalar radiation which becomes highly stretched out in time, during the dispersive propagation to Earth. As observed from a detector on Earth, the GW signal is quasimonochromatic with slowly evolving frequency and amplitude given by Eqs. (53) and (57), respectively. In this section we discuss the detectability of these signals by ground-based GW detectors such as LIGO [67] and Virgo [68]. This should help guide future efforts to search for such signals thereby testing MST gravity. Additionally, and as will be shown below, the absence of any current detection may already be sufficient to place more stringent constraints on the parameters of MST gravity than existing techniques. (For a discussion of existing constraints see, for example, Ref. [35] and references therein.) However, a detailed analysis of the constraints implied by existing measurements is deferred to a future study.

Ground-based GW detectors routinely search for quasi-monochromatic, continuous GW signals (for a recent review, see [69]). The primary motivation for such searches is the possibility of detecting GWs from rapidly rotating, asymmetric neutron stars. Here we hope to leverage these efforts for another purpose, to test a specific class of modified theories of gravity, namely MST gravity. Continuous GW searches fall into three broad classes: (i) *all-sky* searches (see e.g., [70–72]), (ii) *directed* searches, fixing the sky location to that of a known source (see e.g., [73–75]), and (iii) *targeted* searches fixing the sky location, the frequency, and possibly its time derivative to the corresponding values of a known source (see e.g., [76]). All of (i), (ii), or (iii) can be adapted to search for scalar polarized GWs instead of the usual tensorial polarizations (see e.g., [77,78]). However, only methods (i) or (ii) can be used for our present purpose; we could either search the whole sky for or target the location of an historical supernova in the hope that the signal has been dispersively stretched to such an extent that it still retains a detectable amplitude. Method (ii) is computationally cheaper than (i) and can be sensitive to quieter signals, although method (i) has the obvious advantage of covering the whole sky. As for method (iii), fixing the signal frequency is not applicable here without further theoretical assumptions [this is because the frequency $\Omega(t)$ depends on the unknown mass of the scalar field; see Eq. (53)]. However, one may instead fix the relation between Ω and $\dot{\Omega}$ so as to increase the sensitivity of the search.

In this section we calculate the single-detector optimal signal-to-noise ratio (SNR) of our highly dispersed inverse chirp signals. To estimate the SNR for a network of detectors, the individual SNRs can be added in quadrature. We point out the significance of a multidetector network for being able to distinguish between the polarizations of a scalar signal and a standard tensorial GW. The dispersed scalar field signal at the detector is modeled as a simple sine wave,

$$\varphi(t) = A\sin(\Omega t + \phi_0). \tag{64}$$

Any evolution in the amplitude and frequency is neglected in our SNR estimates as such changes typically occur on timescales much longer than a typical LIGO/Virgo observation run, and (save for strong resonances in the noise spectrum) variations of the noise spectral density over a short frequency interval are smaller than temporal variations due to nonstationarity of the instrument. The scalar field is coupled to the physical metric $g_{\mu\nu}$ via Eq. (2); therefore, oscillations in the scalar field source oscillations in $g_{\mu\nu}$, i.e. GWs. In massless ST theory these GWs are transverse, scalar-polarized, with strain amplitude

$$h_B(t) = 2\alpha_0\varphi(t), \tag{65}$$

sometimes called a breathing mode. In MST theory, there is an additional longitudinal polarization with a smaller amplitude,

$$h_L(t) = \left(\frac{\omega_*}{\Omega}\right)^2 2\alpha_0\varphi(t). \tag{66}$$

The response of a GW interferometer is given by

$$h(t) = F(\theta(t), \phi(t))[h_B(t) - h_L(t)], \tag{67}$$

where $F(\theta, \phi) = \frac{-1}{2}\sin^2\theta\cos 2\phi$ is the interferometer antenna pattern which depends on the sky location (θ, ϕ) of the source in a coordinate system attached to the detector [79,80]. The antenna pattern is identical (up to a sign) for both polarizations implying that they cannot be distinguished. As the detector rotates diurnally due to the motion of the Earth, the coordinates (θ, ϕ), and hence the antenna response, change with time. This periodic dependence of the antenna pattern tends to have an averaging effect; sometimes the source is in a favorable location while later it may cross a zero in the antenna pattern. Therefore, for our simple SNR estimates we use the constant, sky averaged rms value for the antenna pattern,

$$\bar{F} = \sqrt{\iint d\theta d\phi \sin\theta F^2(\theta, \phi)} = \sqrt{4\pi/15}. \tag{68}$$

Combining Eqs. (64)–(68), the effective strain $h(t)$ appearing in the interferometer's output is given by

$$h(t) = 2A\alpha_0\bar{F}[1 - (\omega_*/\Omega)^2]\sin(\Omega t + \phi). \tag{69}$$

Here we neglect any Doppler shift in the source frequency caused by the motion of the Earth as this has a negligible effect on the SNR.

The noise in the instrument (commonly assumed to be stationary and Gaussian) is described by the (one-sided) noise power spectral density $S_n(f)$. The optimal SNR ρ is defined in the Fourier domain by the following integral over frequency f [81]:

$$\rho^2 = 4\int_0^\infty df\frac{|\tilde{h}(f)|^2}{S_n(f)}. \tag{70}$$

For an (approximately) sinusoidal signal $h(t)$, the integrand in this equation has support only at $f = \Omega/(2\pi)$, so that the denominator can be pulled out of the integral as a constant $S_n(\Omega/(2\pi))$. In the limit $T \gg 1/\Omega$, the integral in Eq. (70) can be approximated by a time domain integral (using Parseval's theorem) and evaluated to give

$$\rho \approx \sqrt{\frac{S_o}{S_n(\frac{\Omega}{2\pi})}}, \quad \text{where } S_o = T(A\alpha_0\bar{F})^2\left[1 - \left(\frac{\omega_*}{\Omega}\right)^2\right]^2. \tag{71}$$

In Fig. 9 we plot the quantity $\sqrt{S_o}$ (cross symbols) at specific frequencies as a measure of the signal amplitude for two months of observation and the quantity $\sqrt{S_n(f)}$ (solid curves) as a measure of the instrumental noise; the height of the cross above the curve gives a visual measure of the SNR [cf. Eq. (71) with $f = \Omega/(2\pi)$]. For each simulation a sequence of crosses are plotted corresponding to the same source observed at different (retarded) times t after the original supernova; results are shown for $t = 1, 3, 10, 30, 100, 250, 500,$ and 1000 years. Results are shown for several core collapse simulations using the $s39$ progenitor for different values of the MST theory parameters α_0 and β_0 and for two different choices for the equation of state (EOS1 and EOS3). The general trend is that as time passes the frequency slowly decreases following the inverse chirp formula in Eq. (53) while the amplitude can remain at the same order of magnitude for a very long time after the original supernova. This trend is extremely robust to changes in the properties of the progenitor star; additional results for the progenitors $u39$ and $z39$ (both with EOS1 and EOS3) are shown in Appendix D.

The results in Fig. 9 and Appendix D show that if, for example, $(\alpha_0, \beta_0) = (10^{-2}, -20)$, then with the current LIGO capabilities a galactic supernova at $D = 10$ kpc could have a SNR of $\rho \sim 30$ at ~ 200 Hz in 2 months of observation if observed $t = 3$ years after core collapse. Furthermore, such a source remains detectable in LIGO continuous wave searches for $t \sim 300$ years after the original supernova. With the Einstein Telescope or Cosmic Explorer some signals may reach SNRs of ~ 1000 in just 2 months of observation
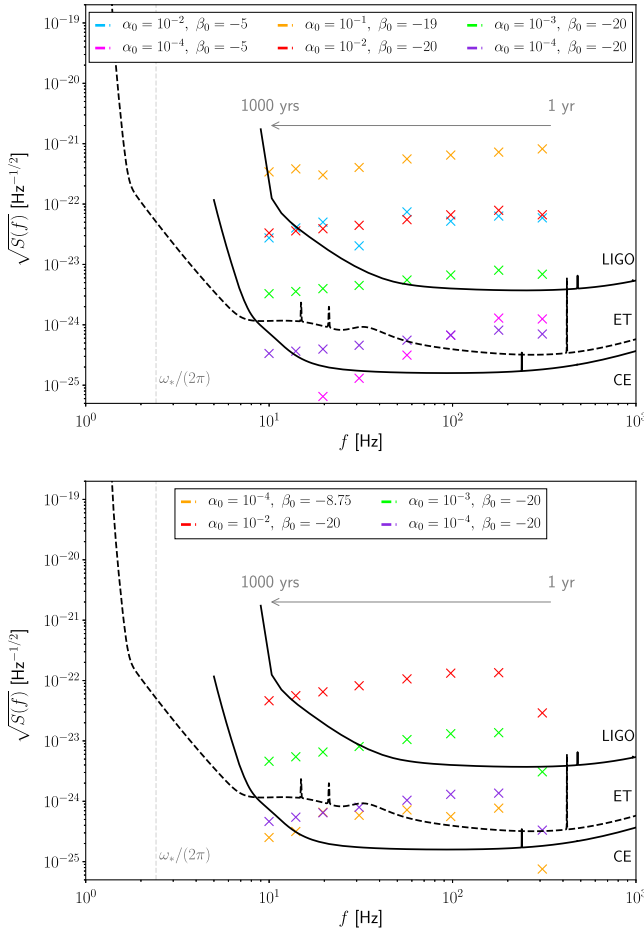
FIG. 9. Signal amplitudes $\sqrt{S_o}$ for quasimonochromatic GWs emitted during stellar collapse for several (α_0, β_0) values with $\mu = 10^{-14}$ eV using progenitor s39 with EOS1 (top) and EOS3 (bottom). These are compared against the expected noise curves $\sqrt{S_n(f)}$ of LIGO [82], the Einstein Telescope, and the Cosmic Explorer [83]. The ratio of $\sqrt{S_o}$ to $\sqrt{S_n(f)}$ gives the SNR which is calculated assuming a 2 month period of observation. Results are shown for observations performed different times after the original supernova: $t = 1$, 3, 10, 30, 100, 250, 500, and 1000 years increasing from right to left on the plot. The signal frequency decreases slowly with t (inverse chirp) while the amplitude remains at the same order of magnitude for up to $t = 1000$ years. These results were computed for a galactic supernova at a distance $D = 10$ kpc from the Earth.

and remain observable for up to 1000 years after the original supernova. Note that the SNR scales with the duration of observation as $\sqrt{T}$ and with distance to the source as $1/D$.

These results are obviously promising for the prospects of making a detection or constraining α_0, β_0, and μ. Because the signals remain detectable for such a long time, it will be worthwhile carrying out directed searches for continuous, scalar-polarized, inverse-chirp signals at the locations of historical supernovae. If such searches yielded no detection, it seems likely that this could be used to place the tightest current constraints on the (α_0, β_0, μ) parameter space of MST

gravity. Supernova 1987A in the large Magellanic cloud is an example of a recent, nearby core-collapse supernova. A detailed projection of the possible constraints are complicated by the μ dependence of the inverse-chirp profile in Eq. (53); we defer a careful analysis of this question to a future study.

VII. CONCLUSIONS

We have performed the first extensive study of spherically symmetric core collapse in MST theory in which we cover a wide range of equations of state and progenitor models, as well as a vast section of the scalar parameter space centered around the threshold for hyperscalarization. A stronger scalar field delays gravitational collapse to the point of impeding BH formation.

For mildly negative values of the quadratic coefficient β_0 in the conformal factor, we recover the two well-known collapse scenarios in GR, the formation of a NS and the formation of a BH resulting from continued accretion onto a proto-NS. For sufficiently negative values of β_0, we encounter three collapse scenarios qualitatively different from those in GR: the formation of a BH following multiple NS stages, the multistage formation of a strongly scalarized NS, and the single-stage formation of a strongly scalarized NS.

The fate of a progenitor (with a fixed equation of state) in GR dictates the distribution of these five collapse scenarios as we vary the scalar parameters. As we change β_0 from zero toward negative values, only two possible successions of collapse scenarios are possible. The first sequence is the following: two-stage BH formation, multistage BH formation, multistage formation of a strongly scalarized NS, single-stage formation of a strongly scalarized NS. The second sequence is single-stage formation of a low-compactness weakly scalarized NS, multistage formation of a strongly scalarized NS, single-stage formation of a strongly scalarized NS. The boundaries between the different classes can vary with the equation of state, the metallicity, or the mass of the progenitor, but for every progenitor we encounter either one or the other sequence, depending on whether the star forms a BH or a NS in GR.

The different scenarios are reflected in the scalar field (which mirrors the matter density evolution) and, as a consequence, in the scalar radiation. The scalar mass causes the GW signal to disperse as it propagates, and by the time it would reach a detector the signal will retain little information with regard to its source, but it carries a highly characteristic imprint of the MST theory. Over a wide range of MST parameters, we find that the resulting gravitational-wave signals will be strong enough to reach SNRs $\gtrsim 20$ over long periods of time, even up to several centuries. This implies potential detection through the study of historical supernovae or, through nondetection, the most stringent constraints on the (α_0, β_0) parameter space of MST theory.

APPENDIX A: COLLAPSE SCENARIOS

In this Appendix, we discuss in more detail the five qualitatively different collapse scenarios listed in Sec. IV A by analyzing for each case a prototypical example. For all configurations discussed in this section, we use a scalar mass $\mu = 10^{-14}$ eV.

1. Single-stage collapse to a weakly scalarized neutron star

The formation of a weakly scalarized neutron star is the scenario realized for weakly (or non-)negative values of β_0 and for equations of state and progenitor models that result in a neutron star in GR. The dynamics of this scenario barely differ from the corresponding collapse in GR and result in a weak GW signal as long as $\alpha_0 \ll 1$.

As an example, we plot in the top row of Fig. 10 as functions of time the central baryon density ρ_c, the central scalar field value φ_c, and the wave signal $\sigma = r_{\mathrm{ex}}\varphi$ at $r_{\mathrm{ex}} = 3 \times 10^4$ km for the collapse of an s39 progenitor with EOS3 and ST parameters $\alpha_0 = 10^{-3}$, $\beta_0 = -2$. This example displays all the characteristics we observe in
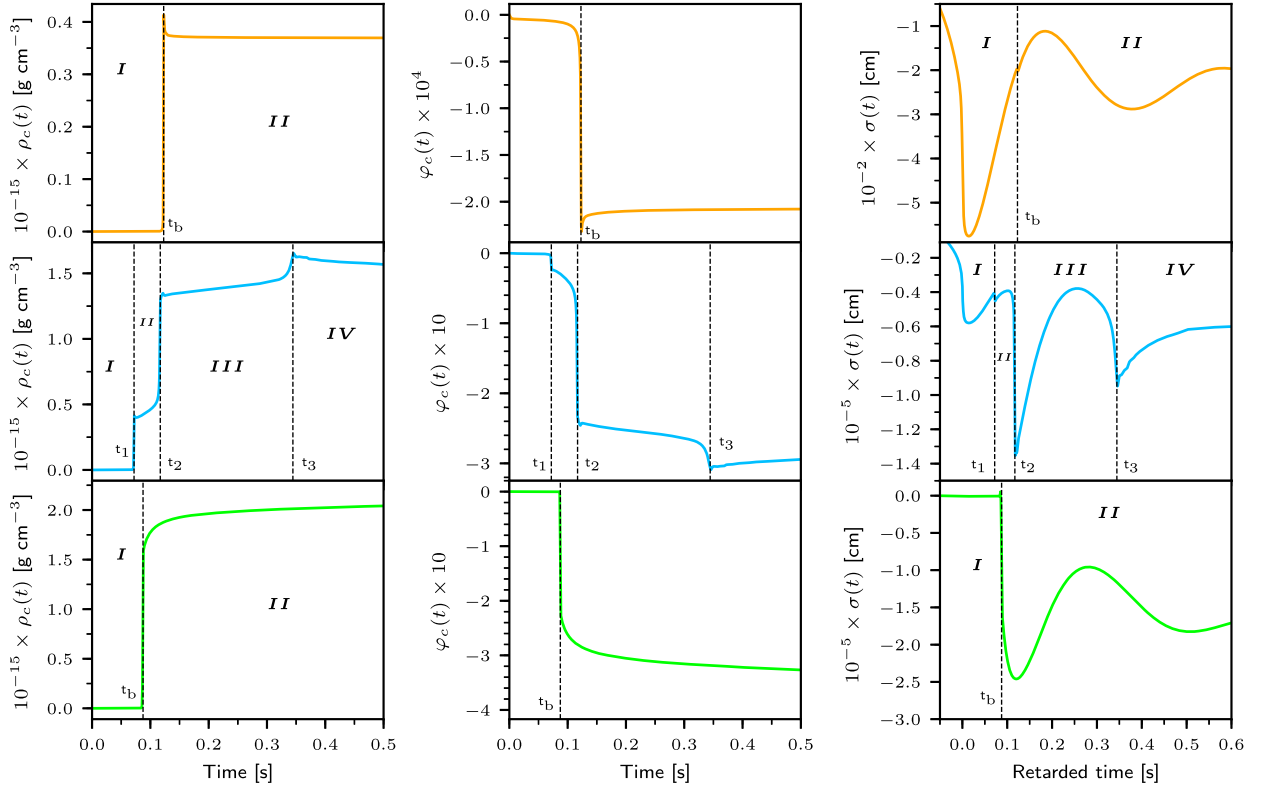

FIG. 10. The central baryon density ρ_c (left), the central scalar field value φ_c (middle), and the wave signal $\sigma = r_{\mathrm{ex}}\varphi$ extracted at $r_{\mathrm{ex}} = 3 \times 10^4$ km (right column) are shown as a function of time for three configurations. *Top*: Progenitor s39 with EOS3 and scalar parameters $\alpha_0 = 10^{-3}$, $\beta_0 = -2$ promptly forms a weakly scalarized NS. *Center*: Progenitor s39 with EOS1 and $\alpha_0 = 10^{-1}$, $\beta_0 = -7$ undergoes a multistage collapse to a strongly scalarized NS. *Bottom*: Progenitor z39 with EOS1 and $\alpha_0 = 10^{-3}$, $\beta_0 = -20$ promptly collapses into a strongly scalarized NS. The Roman numerals label separate stages in the time evolution.

configurations collapsing in a single stage into a weakly scalarized NS. The central density abruptly increases in one jump up to a few times 10^{14} g/cm^3. For nonzero α_0 the jump in density is accompanied by a sudden change in the central scalar field away from zero, but the scalar field only reaches an amplitude $\varphi_c = \mathcal{O}(\alpha)$; cf. the top center panel in Fig. 10. This weak scalarization leads to a correspondingly weak GW signal as shown in the top right panel of the figure.

2. Two-stage formation of a black hole

In the GR limit, a larger ZAMS mass, a lower metallicity, or a softer equation of state may result in the formation of a BH instead of a NS. For non-negative or mildly negative values of β_0, this occurs in two stages; the configuration briefly settles down into a weakly scalarized NS before a second contraction phase results in the final BH (as in GR). In the top row of Fig. 11, we show as an example the progenitor u39 with EOS1 and ST parameters $\alpha_0 = 10^{-3}$, $\beta_0 = -2$. The upper left panel illustrates that the central density first jumps to nuclear values $\mathcal{O}(10^{14})$ g/cm^3 and briefly levels off before a second jump signals the formation of a BH at $t \approx 0.35$ s. The first contraction phase only leads to a weak scalarization and a correspondingly weak GW signal in the center and right panels. The scalarization in the second contraction phase is more complicated; as the stellar compactness increases, the scalar field rapidly strengthens. This increase is halted, however, once a horizon forms and the BH descalarizes in

accordance with the no-hair theorems. The maximal degree of the scalarization critically depends on how rapidly a BH forms and, thus, exhibits sensitive dependence on the configuration's parameters. In our set of simulations, we have found that all degrees from weak to strong scalarization and GW emission are possible in the two-stage BH formation category and that even tiny changes in a parameter can drastically modify the ensuing GW signal; see, for example, the right panel in Fig. 3 where the dark "two-stage BH" region in the (α_0, β_0) plane of the bottom plot covers the entire range of scalarization displayed in the center plot. Among the five qualitatively different collapse scenarios, the two-stage BH formation is the only one that exhibits such a sensitive dependence on the parameters.

3. Multistage collapse to a black hole

This scenario also leads to the formation of a BH, but the collapsing star settles down into at least two temporarily stationary neutron-star configurations with increasing central density. Furthermore, all but the first neutron-star stages are strongly scalarized, so that this scenario always generates a strong GW signal. As an example, we show in the bottom row of Fig. 11 for a progenitor u39 with EOS1 and ST parameters $\alpha_0 = 10^{-3}$, $\beta_0 = -5$ the central density ρ_c, the central scalar field φ_c, and the wave signal $\sigma = r_{\mathrm{ex}}\varphi$ at $r_{\mathrm{ex}} = 3 \times 10^4$ km as functions of time. Note the similarity at early times to the otherwise identical configuration with $\beta_0 = -2$ shown in the upper panel of the same figure. The key
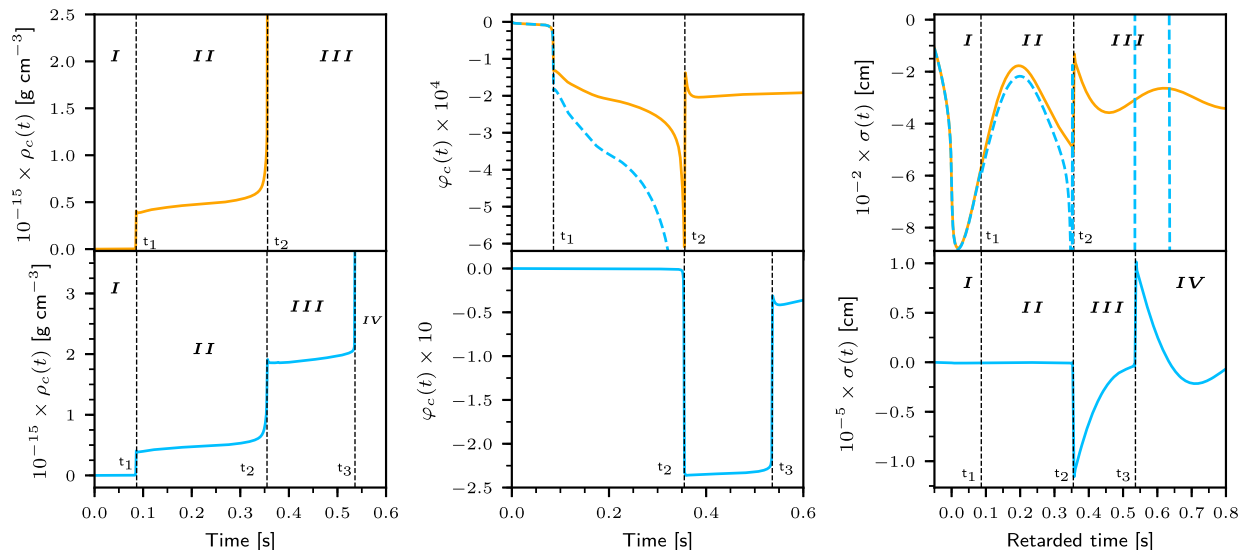

FIG. 11.   The central baryon density ρ_c (left), the central scalar field value φ_c (middle), and the wave signal $\sigma = r_{\mathrm{ex}}\varphi$ extracted at $r_{\mathrm{ex}} = 3 \times 10^4$ km (right column) are shown as a function of time for two configurations. *Top*: The progenitor u39 with EOS1 and scalar parameters $\alpha_0 = 10^{-3}$, $\beta_0 = -2$ temporarily forms a weakly scalarized NS before it collapses to BH at $t \approx 0.35$ s. *Bottom*: The same configuration with $\beta_0 = -5$ also collapses into a BH eventually, but not before briefly settling down into a strongly scalarized NS phase between $t \approx 0.35$ s and $t \approx 0.54$ s. For comparison, the scalar field and wave signal of the second configuration are also displayed as dashed lines in the upper panels. Note how the additional strongly scalarized NS stage leads to an increase in the GW signal by several orders of magnitude.

difference is that the second contraction phase around $t \approx$ 0.35 s promptly results in a BH if $\beta_0 = -2$ but leads to an intermittent strongly scalarized NS phase if $\beta_0 = -5$.

In Fig. 12 we show snapshots of the radial profiles of the baryon density ρ_c and the scalar field φ for this model with $\beta_0 = -5$. Each contraction to a temporarily NS stage is accompanied by the formation of an outgoing shock through core bounce; these are visible at times $t \approx 0.086$ s and $t \approx$ 0.356 s in the profiles $\rho(r)$ in the left panel of the figure. The first NS is weakly scalarized, and we only see a significant increase in the scalar field amplitude in the right panel following the second contraction phase at $t \approx 0.356$ s. The third and final contraction at $t \approx 0.537$ s leads to a BH and, in accordance with the no-hair theorems, the descalarization of the compact star. This strong scalarization and ensuing descalarization results in the two peaks in the GW signal of this configuration in the bottom right panel of Fig. 11.

4. Multistage collapse to a neutron star

This scenario resembles in many ways the multistage formation of a BH discussed in the preceding subsection. Again, we observe a first contraction phase resulting in a weakly scalarized NS followed by one or more further contraction stages. The key difference is that the end product is a highly compact, strongly scalarized NS rather than a BH. An example of this scenario is given by the collapse of the s39 progenitor with EOS1 and ST parameters $\alpha_0 = 10^{-1}$, $\beta_0 = -7$ in the center row of Fig. 10. This configuration reveals three contraction phases that are also visible in the snapshots of the radial profiles of the baryon density ρ and the scalar field φ in Fig. 13.

Again, we observe each contraction phase to result in a core bounce and an outgoing shock visible in the left panel of Fig. 13: The first shock forms at $t \approx 0.072$ s, the second at $t \approx 0.117$ s, while the third discontinuity is weak and barely visible at $t = 0.345$ s around $r \approx 15$ km. As in the case of a multistage BH formation, the significant jumps in the scalar field may result in multiple peaks in the wave signal as shown in the center-right panel of Fig. 10.

5. Single-stage collapse to a strongly scalarized neutron star

The single-stage formation of a strongly scalarized NS can be regarded as the limit of the preceding multistage NS formation with the duration of all intermediate quasistationary NS configurations shrinking to zero. This is indeed what is observed if we start with a given multistage NS model, such as the one discussed in the previous subsection, and then amplify β_0 to increasingly negative values; the lifetime of the intermittent stages decreases, and we approach a single contraction phase to a strongly scalarized NS. This is illustrated for the case of progenitor z39 with EOS1 and ST parameters $\alpha_0 = 10^{-3}$, $\beta_0 = -20$, $\mu = 10^{-14}$eV in Fig. 14 where the snapshots of the baryon density and the scalar profile exhibit one contraction phase accompanied by a rapid increase in scalarization. Over the parameter range we have considered, this scenario ubiquitously represents the limiting scenario for highly negative values of β_0; cf. Fig. 3. The wave signal always consists of a single strong peak for these configurations.
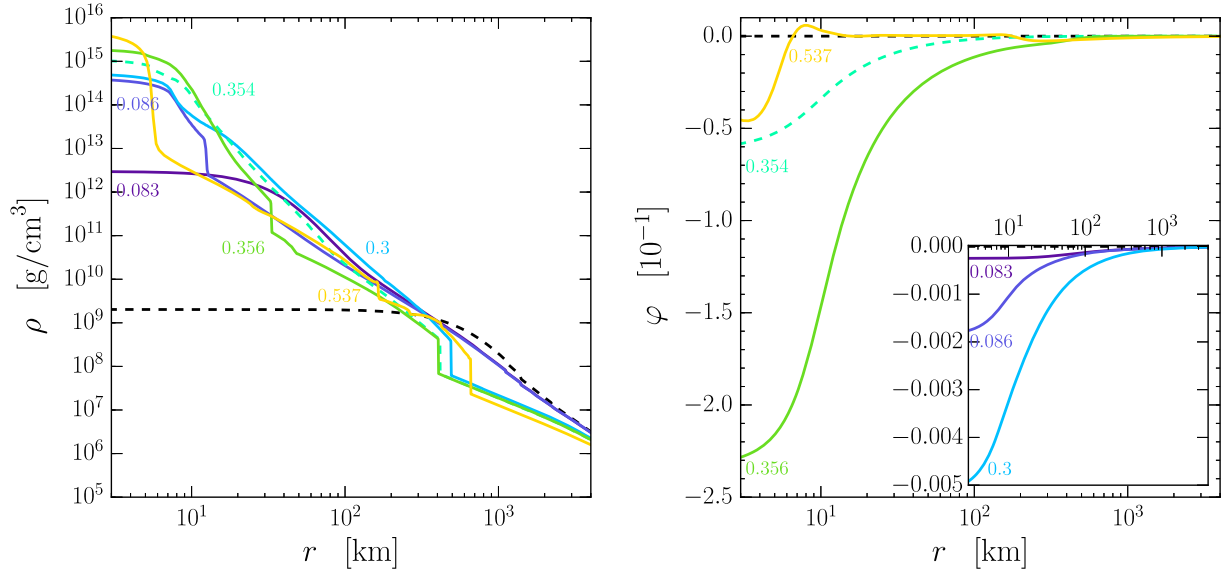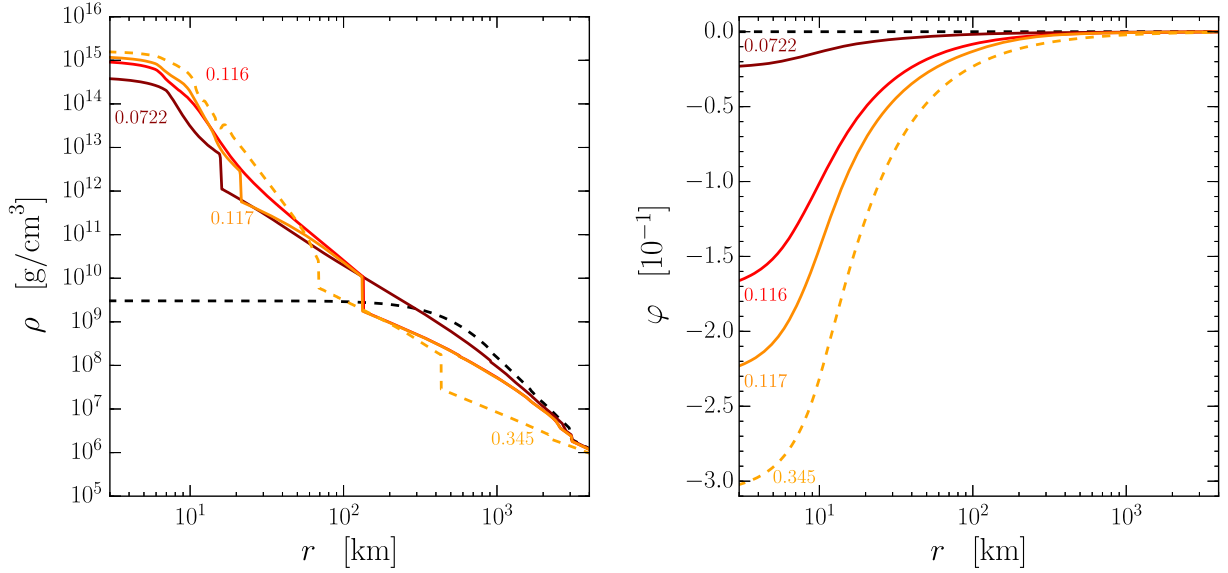

FIG. 12.   Snapshots of the baryon density and scalar field profiles in the collapse of the progenitor u39 with EOS1 and ST parameters $\alpha_0 = 10^{-3}$, $\beta_0 = -5$. The dashed curves show the initial data. A first outgoing shock results from the core bounce at $t \approx 0.086$ s. The second contraction leads to a second core bounce at $t \approx 0.356$ s, and this time the scalar field also increases in amplitude (left panel), signaling the temporary formation of a strongly scalarized NS. At $t \approx 0.537$ s, the baryon density once again starts increasing sharply, this time leading to the formation of a BH and the corresponding descalarization.

FIG. 13. Snapshots of the baryon density and scalar field profiles in the collapse of the progenitor s39 with EOS1 and ST parameters $\alpha_0 = 10^{-1}, \beta_0 = -7$. The dashed curves show the initial data. A first outgoing shock results from the core bounce at $t \approx 0.072$ s. The second contraction leads to a second core bounce at $t \approx 0.116$ s, and this time the scalar field also increases in amplitude (left panel), signaling the temporary formation of a strongly scalarized NS. At $t \approx 0.345$ s, both the baryon density and the scalar field amplitude once again jump, but by lesser margins. Close inspection of the data shows a mild shock that is barely perceptible in the density profile at $t = 0.345$ s around $r \approx 15$ km.
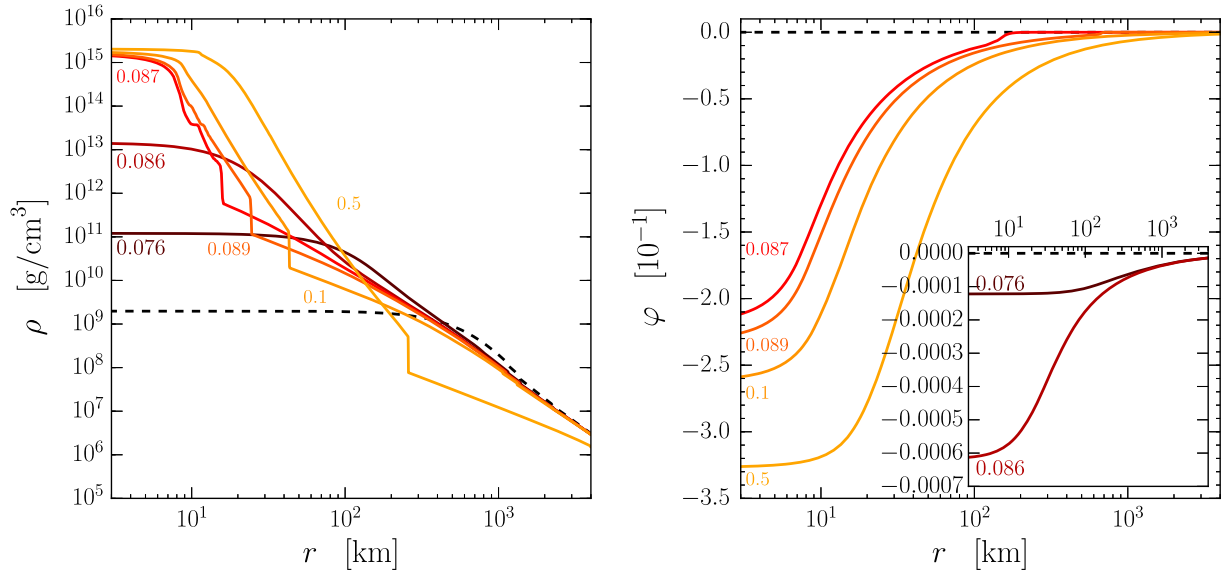
FIG. 14. Snapshots of the baryon density (left) and scalar field (right) profiles during the simulation of a single-stage high-compactness NS. The progenitor is $z39$ with EOS1, and the scalar parameters are $\alpha_0 = 10^{-3}$, $\beta_0 = -20$, and $\mu = 10^{-14}$ eV. The dotted black line represents the initial profile. In this case, core bounce occurs at $t \approx 0.087$ s which leads to a shock propagating outwards. Over the remaining duration of the simulation no further shocks appear and the central density barely changes.

APPENDIX B: ADDITIONAL CLASSIFICATION FOR SEVERAL EQUATIONS OF STATE AND PROGENITOR MODELS

Figures 15 and 16 show additional results to accompany the discussion in Sec. IV A obtained with different stellar progenitors and equations of state. The main conclusion is that every progenitor model results in heat maps in the (α_0, β_0) plane qualitatively equal to that of the neutron star case (left panel of Fig. 3) or that of the black hole case (right panel of Fig. 3).
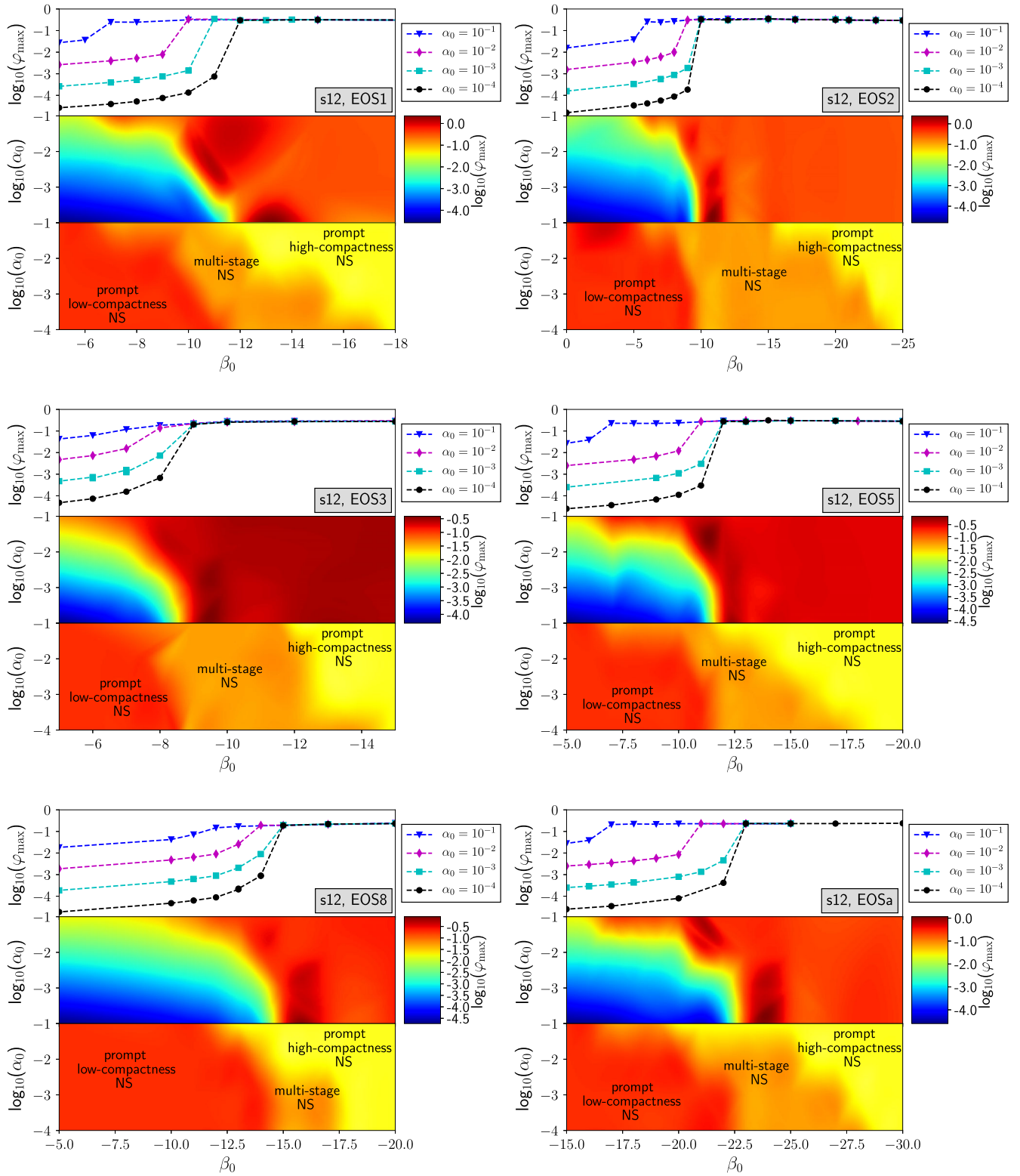
FIG. 15.   Similar to Fig. 3, for each panel we consider a fixed progenitor star with ZAMS mass 12 $M_\odot$, solar metallicity, and several equations of state of Table I. Top rows: For selected values of α_0, we plot the maximal scalarization of the star as a function of β_0. The middle rows provide a color (or "heat") map of the same quantity in the (α_0, β_0) plane: "Red" = strong scalarization, and "Blue" = weak scalarization. The bottom rows present a color code of the five qualitatively different collapse scenarios listed in Sec. IV A. Note that all progenitor models displayed here result in heat maps in the (α_0, β_0) plane qualitatively equal to that on the left side of Fig. 3 (the neutron star case).
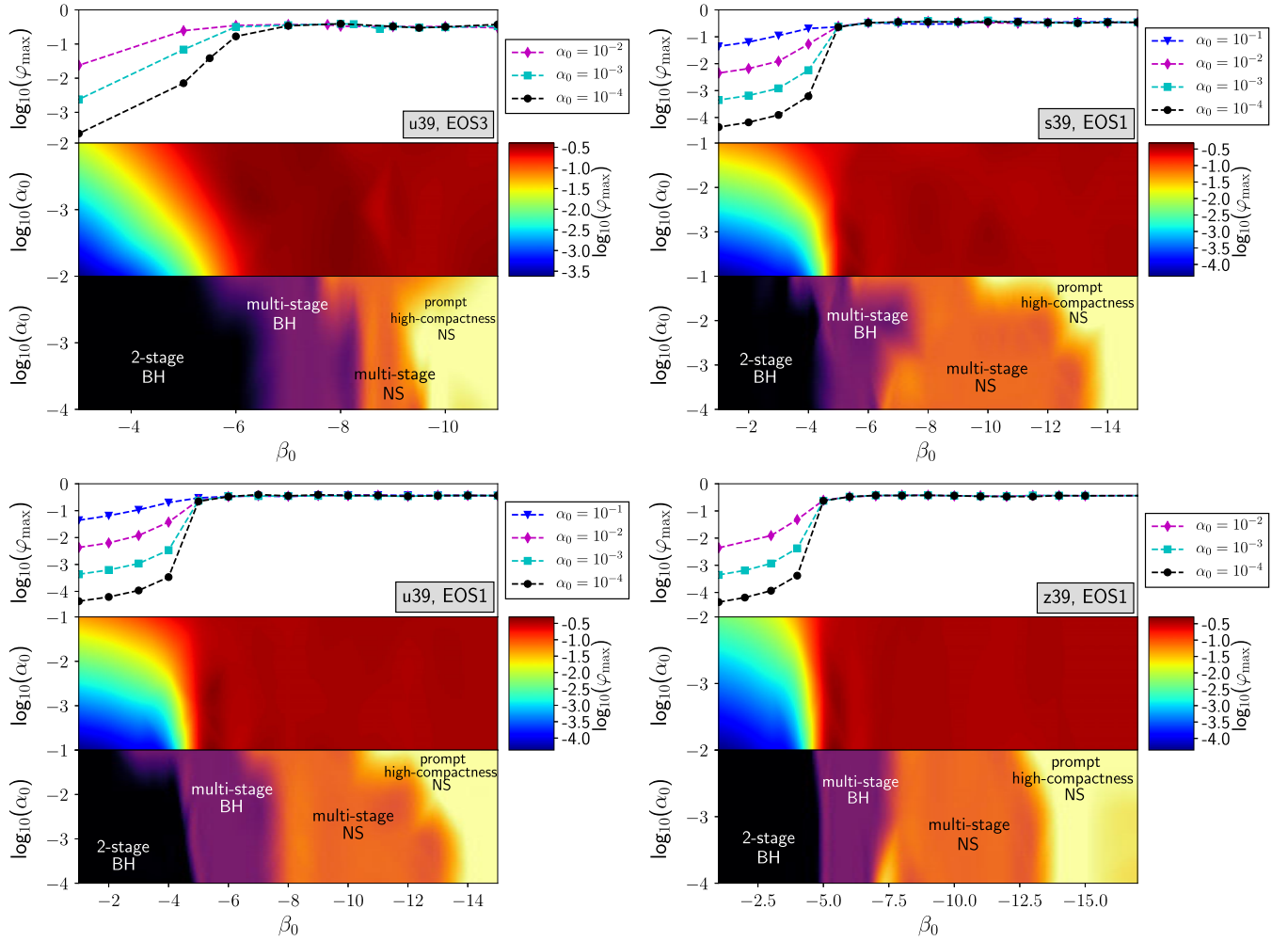
FIG. 16. Similar to Fig. 3, for each panel we consider a fixed progenitor star with ZAMS mass 39 $M_\odot$, all three metallicities and equations of state EOS1 and EOS3 of Table I. Top rows: For selected values of α_0, we plot the maximal scalarization of the star as a function of β_0. The middle rows provides a color (or "heat") map of the same quantity in the (α_0, β_0) plane: "Red"=strong scalarization, and "Blue"=weak scalarization. The bottom rows present a color code of the five qualitatively different collapse scenarios listed in Sec. IV A. Note that all progenitor models displayed here result in heat maps in the (α_0, β_0) plane qualitatively equal to that on the right side of Fig. 3 (the black hole case).

APPENDIX C: COMPARING THE METHODS

This Appendix contains a test and comparison of the two methods described in Secs. V A and V B for propagating signals from the extraction sphere to larger radii. For this test, consider a simple signal which, on the extraction sphere, is a cosine-Gaussian wave packet:

$$\sigma(u; r_{\rm ex}) = \cos\left(\frac{2\pi(u - r_{\rm ex})}{T}\right) \exp\left(\frac{-(u - r_{\rm ex})^2}{18T^2}\right). \quad (C1)$$

The parameter T is an overall timescale which is set to unity without loss of generality and the scalar field mass was chosen to be $\omega_* = 2/T$. The signal was propagated to larger radii using both of the methods described in Secs. V A and V B, and the results are summarized in Fig. 17.

As can be seen from Fig. 17, there is excellent qualitative agreement between the two methods. At the quantitative level there are small errors (generally $\lesssim 1\%$, as can be seen from the lower panel) which are due to numerical errors in the $1 + 1$ time domain evolution (this has been checked by verifying the scaling of the errors with grid resolution). As the signals propagate to larger radii, the peak lags at later retarded times due to the subluminal wave propagation. Additionally, the variation in the group velocity between the different Fourier components of the wave packet leads to a broadening of the peak; careful inspection of the $\sigma(u; r_2)$ profile reveals the beginnings of an *inverse chirp* profile (see Sec. V C) where the high frequencies arrive first, followed by the low frequencies.
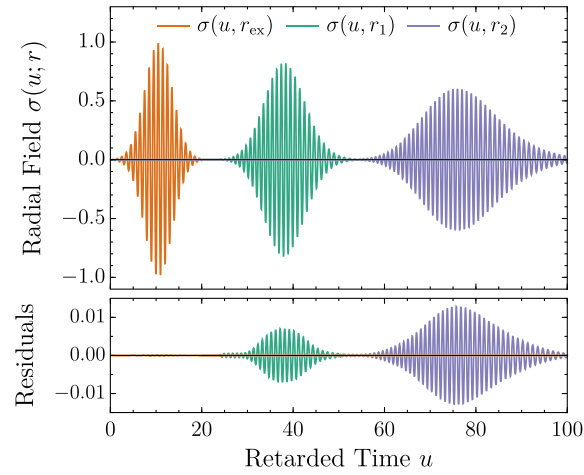
FIG. 17.   The top panel shows the results of evolving an initially sin-Gaussian waveform out to radii $r_1 = r_{ex} + 500cT$ and $r_2 = r_{ex} + 1200cT$ using the time domain numerical evolution of the wave equation (see Sec. V A). The evolution to large radii was also performed using the analytic Fourier domain approach (see Sec. V B), and the bottom panel shows the differences, or residuals, between the two methods.

APPENDIX D: ADDITIONAL SNR RESULTS

Figures 18 and 19 show additional results to accompany the discussion in Sec. VI obtained with different stellar progenitors. The main conclusion is that the properties of the progenitor have only a mild effect on the SNR.
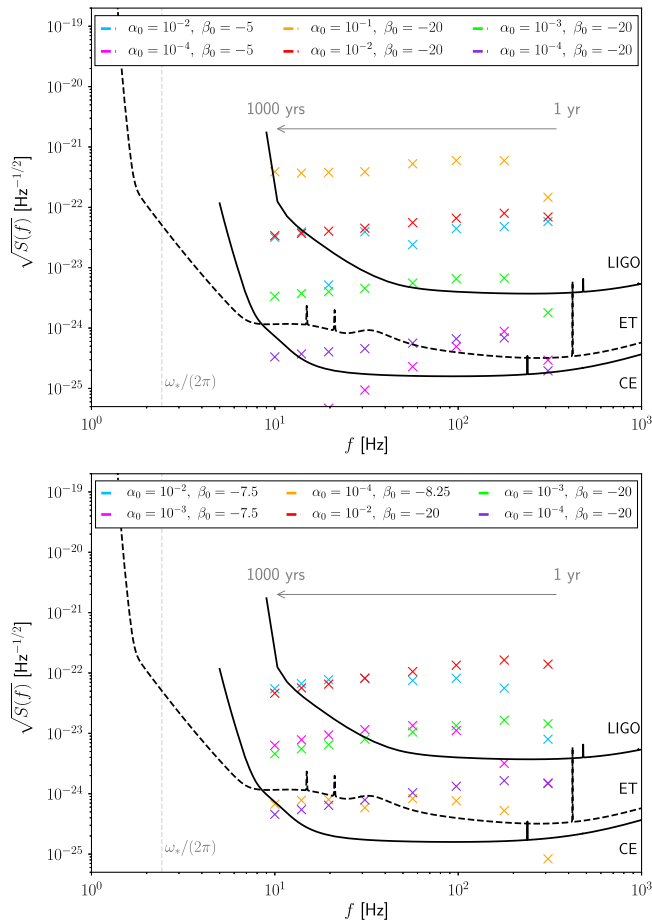

FIG. 18.   Similar to Fig. 9, but for stellar collapse of the $u39$ progenitor model.
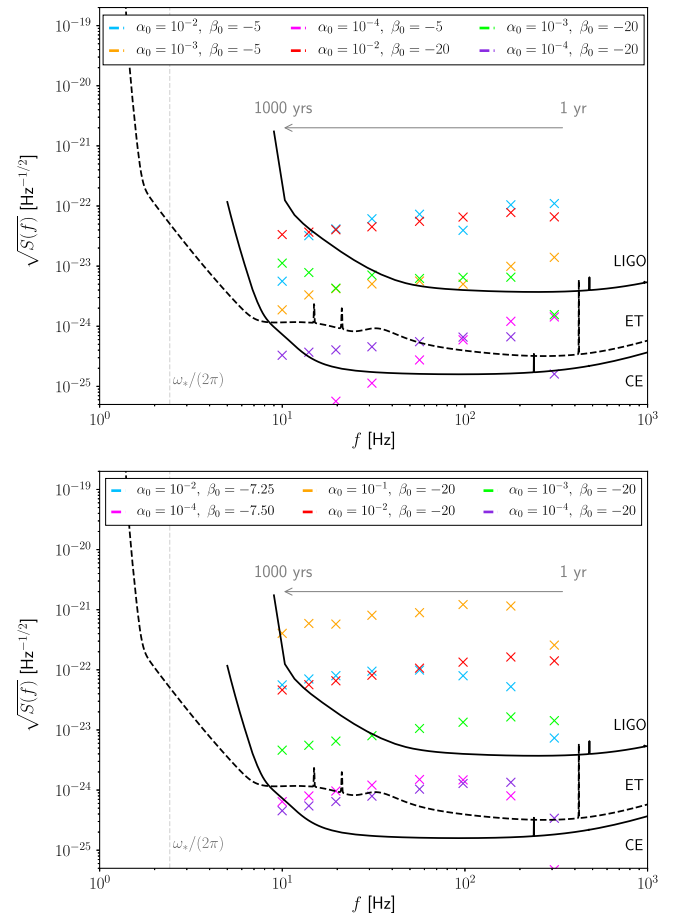

FIG. 19.   Similar to Fig. 9, but for stellar collapse of the $z39$ progenitor model.

[1] E. Berti et al., Classical Quantum Gravity **32,** 243001 (2015).

[2] T. Damour and G. Esposito-Farese, Phys. Rev. Lett. **70,** 2220 (1993).

[3] F. M. Ramazanoğlu and F. Pretorius, Phys. Rev. D **93,** 064005 (2016).

[4] D. D. Doneva, S. S. Yazadjiev, N. Stergioulas, and K. D. Kokkotas, Phys. Rev. D **98,** 104039 (2018).

[5] N. Andreou, N. Franchini, G. Ventagli, and T. P. Sotiriou, Phys. Rev. D **99,** 124022 (2019).

[6] H. O. Silva, J. Sakstein, L. Gualtieri, T. P. Sotiriou, and E. Berti, Phys. Rev. Lett. **120,** 131104 (2018).

[7] D. D. Doneva and S. S. Yazadjiev, Phys. Rev. Lett. **120,** 131103 (2018).

[8] E. Barausse, T. Jacobson, and T. P. Sotiriou, Phys. Rev. D **83,** 124043 (2011).

[9] F. M. Ramazanoğlu, Phys. Rev. D **96,** 064009 (2017).

[10] F. M. Ramazanoğlu, Phys. Rev. D **99,** 084015 (2019).

[11] L. Annulli, V. Cardoso, and L. Gualtieri, Phys. Rev. D **99,** 044038 (2019).

[12] Y. Foures-Bruhat, Acta Mat. **88,** 141 (1952).

[13] Y. Choquet-Bruhat and R. P. Geroch, Commun. Math. Phys. **14,** 329 (1969).

[14] M. Salgado, D. Martinez-del Rio, M. Alcubierre, and D. Nunez, Phys. Rev. D **77,** 104010 (2008).

[15] T. Delsate, D. Hilditch, and H. Witek, Phys. Rev. D **91,** 024027 (2015).

[16] G. Papallo and H. S. Reall, Phys. Rev. D **96,** 044019 (2017).

[17] G. Papallo, Phys. Rev. D **96,** 124036 (2017).

[18] G. Papallo, Causality and the initial value problem in Modified Gravity, Ph.D. thesis, Cambridge University, DAMTP, 2018.

[19] C. Brans and R. H. Dicke, Phys. Rev. **124,** 925 (1961).

[20] G. W. Horndeski, Int. J. Theor. Phys. **10,** 363 (1974).

[21] B. Bertotti, L. Iess, and P. Tortora, Nature (London) **425,** 374 (2003).

[22] J. G. Williams, S. G. Turyshev, and D. H. Boggs, Int. J. Mod. Phys. D **18,** 1129 (2009).

[23] N. Wex, arXiv:1402.5594.

[24] N. Yunes, K. Yagi, and F. Pretorius, Phys. Rev. D **94,** 084002 (2016).

[25] B. P. Abbott et al. (LIGO and Virgo Collaborations), Phys. Rev. D **100,** 104036 (2019).

[26] B. P. Abbott et al. (LIGO and Virgo Collaborations; Electromagnetic Partners), Astrophys. J. **848,** L12 (2017).

[27] J. M. Ezquiaga and M. Zumalacárregui, Phys. Rev. Lett. **119,** 251304 (2017).

[28] J. Sakstein and B. Jain, Phys. Rev. Lett. **119,** 251303 (2017).

[29] P. Creminelli and F. Vernizzi, Phys. Rev. Lett. **119,** 251302 (2017).

[30] P. G. Bergmann, Int. J. Theor. Phys. **1,** 25 (1968).

[31] R. V. Wagoner, Phys. Rev. D **1,** 3209 (1970).

[32] J. Novak, Phys. Rev. D **58,** 064019 (1998).

[33] J. Novak, Phys. Rev. D **57,** 4789 (1998).

[34] J. Novak and J. M. Ibanez, Astrophys. J. **533,** 392 (2000).

[35] D. Gerosa, U. Sperhake, and C. D. Ott, Classical Quantum Gravity **33,** 135002 (2016).

[36] R. F. P. Mendes and N. Ortiz, Phys. Rev. D **93,** 124035 (2016).

[37] U. Sperhake, C. J. Moore, R. Rosca, M. Agathos, D. Gerosa, and C. D. Ott, Phys. Rev. Lett. **119,** 201103 (2017).

[38] P. C.-K. Cheong and T. G. F. Li, Phys. Rev. D **100,** 024027 (2019).

[39] R. Rosca-Mead, C. J. Moore, M. Agathos, and U. Sperhake, Classical Quantum Gravity **36,** 134003 (2019).

[40] C.-Q. Geng, H.-J. Kuan, and L.-W. Luo, arXiv:2005.11629.

[41] M. Salgado, Classical Quantum Gravity **23,** 4719 (2006).

[42] V. Faraoni and E. Gunzig, Int. J. Theor. Phys. **38,** 217 (1999).

[43] C.-Q. Geng, H.-J. Kuan, and L.-W. Luo, Classical Quantum Gravity **37,** 115001 (2020).

[44] Y. Fujii and K. Maeda, The Scalar-Tensor Theory of Gravitation, Cambridge Monographs on Mathematical Physics (Cambridge University Press, Cambridge, England, 2007).

[45] T. Damour and G. Esposito-Farese, Classical Quantum Gravity **9,** 2093 (1992).

[46] T. Damour and G. Esposito-Farese, Phys. Rev. D **54,** 1474 (1996).

[47] T. Chiba, T. Harada, and K.-i. Nakao, Prog. Theor. Phys. Suppl. **128,** 335 (1997).

[48] J. M. Bardeen, in Gravitational Radiation, edited by T. Deruelle and N. Piran (North-Holland, Amsterdam, 1983), pp. 433–441.

[49] E. O'Connor and C. D. Ott, Classical Quantum Gravity **27,** 114103 (2010).

[50] H. T. Janka, T. Zwerger, and R. Moenchmeyer, Astron. Astrophys. **268,** 360 (1993).

[51] T. Zwerger and E. Mueller, Astron. Astrophys. **320,** 209 (1997).

[52] H. Dimmelmeier, J. A. Font, and E. Muller, Astron. Astrophys. **393,** 523 (2002).

[53] H. Dimmelmeier, C. D. Ott, H.-T. Janka, A. Marek, and E. Mueller, Phys. Rev. Lett. **98,** 251101 (2007).

[54] H. Dimmelmeier, C. D. Ott, A. Marek, and H. T. Janka, Phys. Rev. D **78,** 064056 (2008).

[55] S. L. Shapiro and S. A. Teukolsky, Black Holes, White Dwarfs, and Neutron Stars: The Physics of Compact Objects (John Wiley & Sons, Inc., New York, 1983).

[56] H. Shen, H. Toki, K. Oyamatsu, and K. Sumiyoshi, Astrophys. J. Suppl. Ser. **197,** 20 (2011).

[57] J. M. Lattimer, C. J. Pethick, D. G. Ravenhall, and D. Q. Lamb, Nucl. Phys. **A432,** 646 (1985).

[58] J. M. Lattimer and F. Douglas Swesty, Nucl. Phys. **A535,** 331 (1991).

[59] H. Shen, H. Toki, K. Oyamatsu, and K. Sumiyoshi, Prog. Theor. Phys. **100,** 1013 (1998).

[60] H. Shen, H. Toki, K. Oyamatsu, and K. Sumiyoshi, Nucl. Phys. **A637,** 435 (1998).

[61] S. E. Woosley and A. Heger, Phys. Rep. **442,** 269 (2007).

[62] E. O'Connor and C. D. Ott, Astrophys. J. **730,** 70 (2011).

[63] K. S. Thorne and J. J. Dykla, Astrophys. J. Lett. **166,** L35 (1971).

[64] S. W. Hawking, Commun. Math. Phys. **25,** 167 (1972).

[65] M. W. Choptuik, Phys. Rev. Lett. **70,** 9 (1993).

[66] S. A. Teukolsky, Phys. Rev. D **61,** 087501 (2000).

[67] J. Aasi et al. (LIGO Scientific Collaboration), Classical Quantum Gravity **32,** 074001 (2015).

[68] F. Acernese *et al.* (Virgo Collaboration), Classical Quantum Gravity **32**, 024001 (2015).

[69] K. Riles, Mod. Phys. Lett. A **32**, 1730035 (2017).

[70] B. P. Abbott *et al.* (LIGO and Virgo Collaborations), Phys. Rev. D **100**, 024004 (2019).

[71] B. P. Abbott *et al.* (LIGO and Virgo Collaborations), Phys. Rev. D **97**, 102003 (2018).

[72] B. P. Abbott *et al.* (LIGO and Virgo Collaborations), Phys. Rev. D **96**, 122004 (2017).

[73] B. P. Abbott *et al.* (LIGO and Virgo Collaborations), Phys. Rev. D **95**, 122003 (2017).

[74] B. P. Abbott *et al.* (LIGO and Virgo Collaborations), Astrophys. J. **847**, 47 (2017).

[75] B. P. Abbott *et al.* (LIGO and Virgo Collaborations), Astrophys. J. **875**, 122 (2019).

[76] B. P. Abbott *et al.* (LIGO and Virgo Collaborations), Astrophys. J. **839**, 12 (2017); **851**, 71(E) (2017).

[77] B. P. Abbott *et al.* (LIGO and Virgo Collaborations), Phys. Rev. Lett. **120**, 031104 (2018).

[78] M. Isi, M. Pitkin, and A. J. Weinstein, Phys. Rev. D **96**, 042001 (2017).

[79] D. Babusci, L. Baiotti, F. Fucito, and A. Nagar, Phys. Rev. D **64**, 062001 (2001).

[80] C. M. Will, Living Rev. Relativity **17**, 4 (2014).

[81] C. J. Moore, R. H. Cole, and C. P. L. Berry, Classical Quantum Gravity **32**, 015014 (2015).

[82] B. Abbott *et al.* (KAGRA, LIGO Scientific, and Virgo Collaborations), Living Rev. Relativity **21**, 3 (2018).

[83] B. P. Abbott *et al.* (LIGO Scientific Collaboration), Classical Quantum Gravity **34**, 044001 (2017).